

Globally coherent water cycle response to temperature change during the past two millennia

Received: 17 November 2022

Accepted: 15 September 2023

Published online: 2 November 2023

 Check for updates

Bronwen L. Konecky¹✉, Nicholas P. McKay¹, Georgina M. Falster^{1,3}, Samantha L. Stevenson⁴, Matt J. Fischer¹, Alyssa R. Atwood¹, Diane M. Thompson¹, Matthew D. Jones¹, Jonathan J. Tyler¹, Kristine L. DeLong¹, Belen Martrat¹, Elizabeth K. Thomas^{1,2}, Jessica L. Conroy¹, Sylvia G. Dee¹, Lukas Jonkers¹, Olga V. Churakova (Sidorova)^{16,17}, Zoltán Kern^{18,19}, Thomas Opel¹, Trevor J. Porter¹, Hussein R. Sayani²², Grzegorz Skrzypek¹, & Iso2k Project Members*

The response of the global water cycle to changes in global surface temperature remains an outstanding question in future climate projections and in past climate reconstructions. The stable hydrogen and oxygen isotope compositions of precipitation (δ_{precip}), meteoric water (δ_{MW}) and seawater (δ_{SW}) integrate processes from microphysical to global scales and thus are uniquely positioned to track global hydroclimate variations. Here we evaluate global hydroclimate during the past 2,000 years using a globally distributed compilation of proxies for δ_{precip} , δ_{MW} and δ_{SW} . We show that global mean surface temperature exerted a coherent influence on global δ_{precip} and δ_{MW} throughout the past two millennia, driven by global ocean evaporation and condensation processes, with lower values during the Little Ice Age (1450–1850) and higher values after the onset of anthropogenic warming (~1850). The Pacific Walker Circulation is a predominant source of regional variability, particularly since 1850. Our results demonstrate rapid adjustments in global precipitation and atmospheric circulation patterns—within decades—as the planet warms and cools.

Recent global syntheses of palaeoclimate ‘proxy’ data have constrained global mean surface temperature (GMST) changes during the past 2,000 years (that is, the Common Era, CE), providing critical context for anthropogenic warming^{1,2}. Yet despite the importance of water resources to society, contemporaneous variations in the global water cycle—including precipitation, evapotranspiration, atmospheric circulation and modes of climate variability that affect these processes—remain underconstrained^{3,4}.

Stable hydrogen and oxygen isotope ratios ($\delta^2\text{H}$ and $\delta^{18}\text{O}$) in environmental waters are well positioned to provide a global picture of

hydroclimate. Evaporation, condensation, freezing and other phase changes in the water cycle differentially impact (fractionate) heavy versus light isotopes, causing the $\delta^2\text{H}$ and $\delta^{18}\text{O}$ of precipitation (δ_{precip}), precipitation-derived meteoric waters such as lake and soil water (δ_{MW}), and seawater (δ_{SW}) to integrate and record hydrological processes on timescales from minutes to millions of years^{5–12}. Variations in δ_{precip} , δ_{MW} and δ_{SW} are subsequently incorporated into diverse geologic materials including speleothem and coral carbonate, glacial ice and tree cellulose. By synthesizing such data from a variety of sources, it is therefore possible to infer changes in a powerful suite of hydroclimatic variables:

A full list of affiliations appears at the end of the paper. ✉ e-mail: bkonecky@wustl.edu

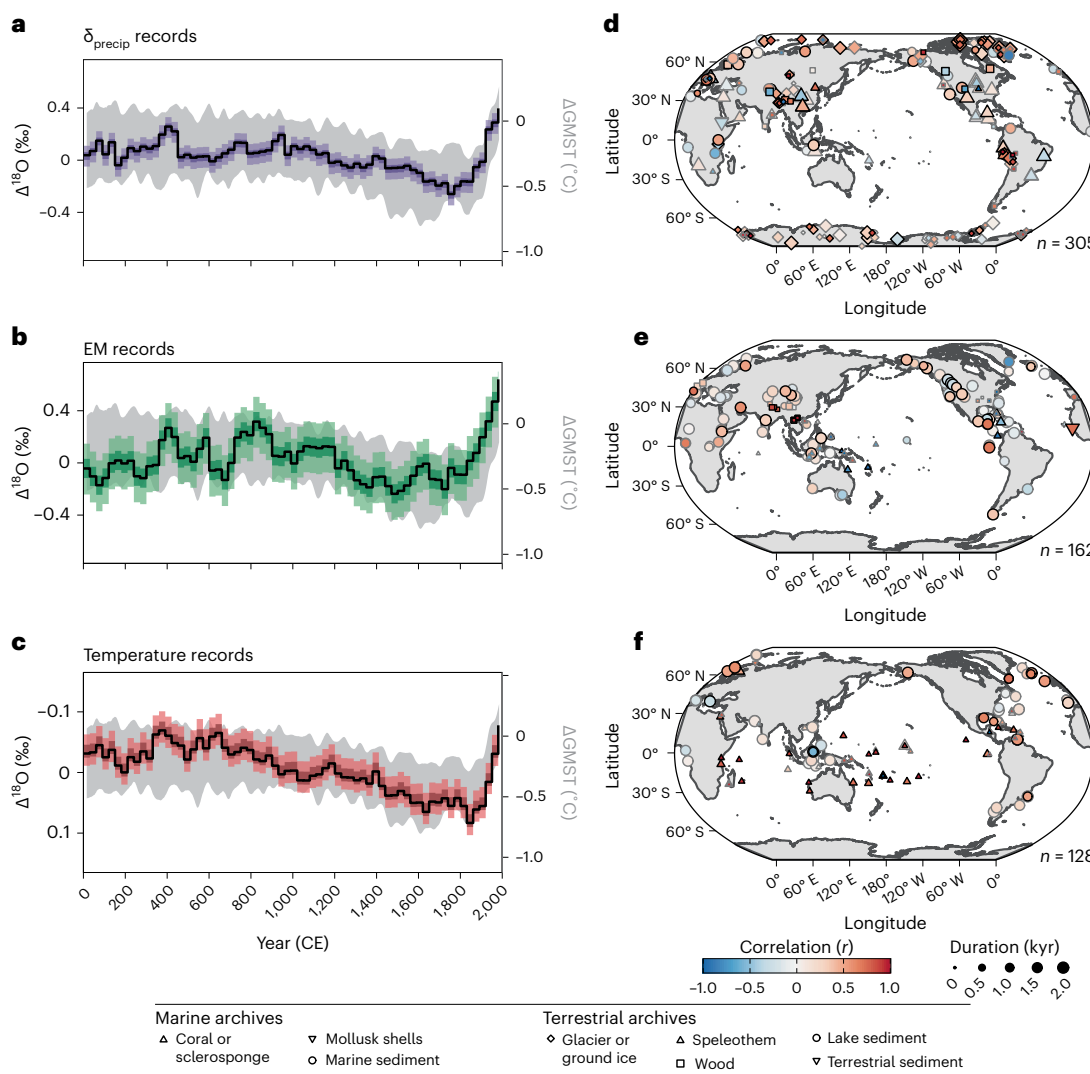


Fig. 1 | Global composite oxygen isotope anomalies. **a–c**, 30-year binned proxy $\Delta^{18}\text{O}$ (black line, ensemble median; dark shading, 25th–75th percentiles; light shading, 2.5th–97.5th percentiles) for each group of Iso2k records¹⁵, anomalies relative to 2,000-year mean. Grey shading depicts ensemble 2.5th–97.5th percentile GMST anomaly relative to 1961–1990 mean¹. Note y-axis in c is reversed

to orient values upwards for warmer periods. **d–f**, Records contributing to each composite. Symbol shape, archive type; size, record duration; shading, correlation between that record and the corresponding composite; bold outline, $P < 0.05$. Correlations are Pearson's r , two-sided, with no adjustment for multiple correlation. Maps created in R, using coastlines from Natural Earth.

δ_{precip} , which reflects atmospheric factors such as condensation temperature, precipitation amount, rainout history and moisture source¹²; δ_{MW} from lake, soil and groundwaters, which reflects variations in δ_{precip} and surface water evaporation; and δ_{SW} , which reflects δ_{precip} , seawater evaporation and mixing^{13,14}.

We analysed proxies for δ_{precip} , δ_{MW} and δ_{SW} from the recently published Past Global Changes (PAGES) Iso2k database, which contains 759 globally distributed palaeoclimate records from coral, tree, ice, speleothem, lake and marine sites¹⁵. The database includes extensive metadata designed to facilitate cross-archive comparison, including interpretations from the original publications and supplemented with information from a team of over 50 archive experts (ref. 15 provides details on database design). Metadata fields include original climatic interpretations, proxy system transformations and the multiple environmental drivers of the isotopic composition of the measured material in each record (hereafter ‘isotope interpretation’). Each record is further classified into one of three primary isotope interpretation groups: (1) δ_{precip} ; (2) effective moisture (EM), that is, the balance between precipitation and evaporation, with higher EM reflecting higher precipitation relative to evaporation; or (3) the in situ temperature of the

environmental medium during the formation of the proxy sensor or archive¹⁵ (we note most records in the temperature category are marine carbonates whose $\delta^{18}\text{O}$ primarily reflects seawater temperature, with only minor influence of δ_{SW} (ref. 16)). Regional and global analyses were performed on these three isotope interpretation groups to distinguish patterns in different reservoirs of the water cycle (precipitation, surface water, seawater), without a priori assumptions about the climatic drivers of each record’s variability (for example, upstream monsoon intensity, regional air temperature), which are more subject to change as records are re-interpreted over time (Methods).

For each group, we created composite records of global $\delta^{18}\text{O}$ anomalies relative to the 0–2000 CE mean ($\Delta^{18}\text{O}$), including $\delta^2\text{H}$ records scaled to $\delta^{18}\text{O}$ -equivalent variance, using a dynamic compositing method that was previously employed to reconstruct palaeotemperature in a manner that robustly handles proxy time series of different lengths, resolutions and coverage periods (ref. 17 and Methods). In addition to calculating composites, we performed principal component analysis (PCA) on a subset of higher-resolution (that is, ≤ 30 -year bins) individual proxy records with $>85\%$ temporal data coverage during the last millennium (LM; 850–1850) to reveal dominant

spatio-temporal modes of variability (Methods). We compared these results to an ensemble of three full-forcing LM experiments with the water isotope-enabled Community Earth System Model (iCESM)^{18–20}.

The three $\Delta^{18}\text{O}$ composites (Fig. 1) display similar patterns, with notable differences in the magnitude of centennial-scale variability. During the first millennium, composite $\Delta^{18}\text{O}$ of δ_{precip} -driven records (hereafter, composite $\Delta^{18}\text{O}_{\delta_{\text{precip}}}$) was relatively stable, whereas composite $\Delta^{18}\text{O}$ of EM- and temperature-driven records (composite $\Delta^{18}\text{O}_{\text{EM}}$ and $\Delta^{18}\text{O}_{\text{temp}}$) increased and decreased, respectively. During the LM, all three composites show a monotonic trend from ~800 to ~1700 and a reversal of that trend since the nineteenth century. These patterns broadly echo the temporal evolution of GMST during the LM¹ but with different magnitudes depending on the primary environmental interpretation of $\delta^{18}\text{O}$. From 1000 to 1850, a global cooling of $0.25 (\pm 0.1)$ °C (ref. 1) corresponds to a change of $-0.27 (\pm 0.00021)$, $+0.02 (\pm 0.00019)$ and $+0.09\text{\textperthousand} (\pm 0.0002)$ in composite $\Delta^{18}\text{O}_{\delta_{\text{precip}}}$, $\Delta^{18}\text{O}_{\text{EM}}$ and $\Delta^{18}\text{O}_{\text{temp}}$, respectively (Fig. 1a–c). Subsequent warming of $0.65 (\pm 0.06)$ °C from 1850 to 2000 corresponds to a change of $+0.56 (\pm 0.00012)$, $+0.62 (\pm 0.00017)$ and $-0.16\text{\textperthousand} (\pm 0.00023)$, respectively. Uncertainties in these estimates are based on differences between the respective time periods across the full ensemble (Methods).

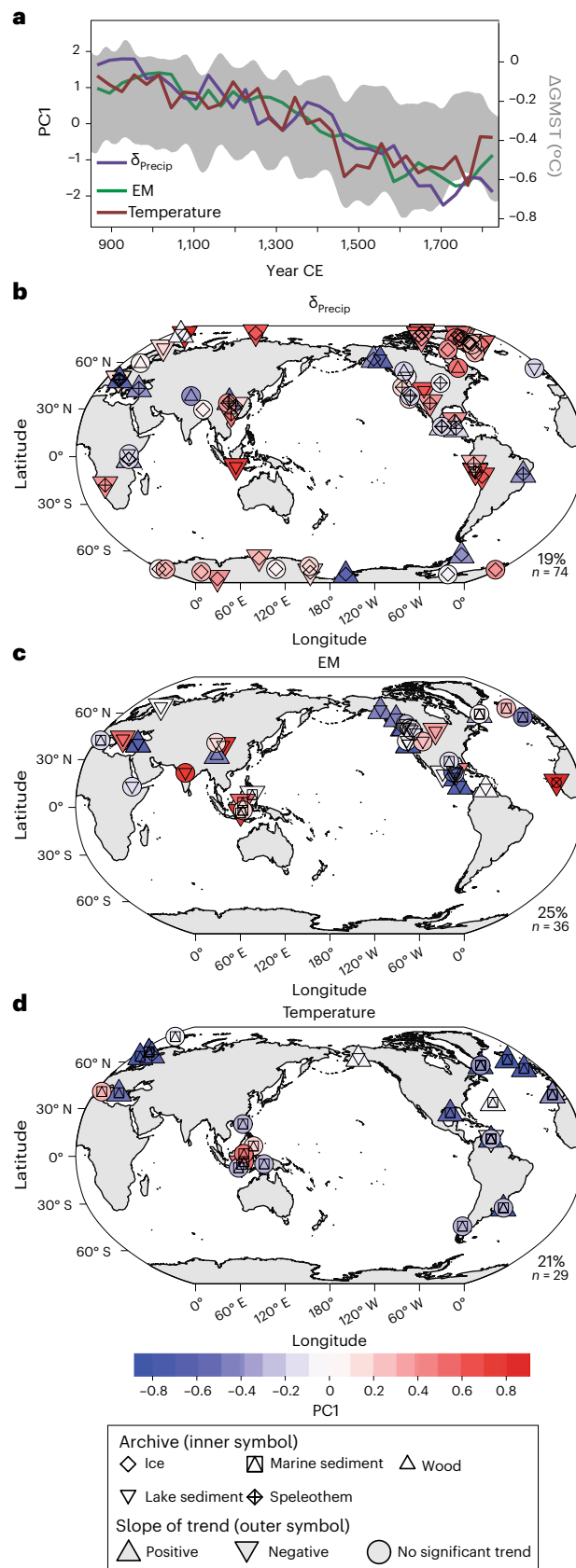
Composite $\Delta^{18}\text{O}_{\text{EM}}$ displays pronounced centennial-scale variability, with distinct positive excursions from 300–500, 700–900 and 1800–2000. Variability in composite $\Delta^{18}\text{O}_{\text{EM}}$ is at least twice the magnitude of composite $\Delta^{18}\text{O}_{\text{temp}}$ or $\Delta^{18}\text{O}_{\delta_{\text{precip}}}$ (Fig. 1), probably due to the strong influence of surface water evaporation on lake and seawater $\delta^{18}\text{O}$, which amplifies the δ_{precip} signal relative to noise^{11,12}.

The first principal component (PC1) of each category of records is dominated by a monotonic trend over the LM, with smaller centennial-scale fluctuations (Fig. 2a). Similar to the composites, the gross trend in each PC1 corresponds to a decrease in GMST. Site loadings on each PC1, however, differ by region and by the primary environmental driver of $\delta^{18}\text{O}$ (Fig. 2b–d). For example, positive trends and negative PC1 loadings are evident in $\delta^{18}\text{O}_{\text{temp}}$ at almost all extra-tropical locations (Fig. 2d), consistent with the impact of ocean cooling on the $\delta^{18}\text{O}$ of marine carbonates. Contrastingly, trends are insignificant in the Indo-Pacific Warm Pool where $\delta^{18}\text{O}_{\text{sw}}$ influence probably confounds the temperature signal²¹.

Influence of temperature on the oxygen isotopic composition of global meteoric waters

Together, the $\Delta^{18}\text{O}$ composites and PC1 suggest that GMST exerts a first-order control on temporal changes in global δ_{MW} during the CE. The relationship of composite $\Delta^{18}\text{O}_{\delta_{\text{precip}}}$ with temperature is $0.68 \pm 0.20\text{\textperthousand} ^\circ\text{C}^{-1}$ for the full CE and $0.78 \pm 0.19\text{\textperthousand} ^\circ\text{C}^{-1}$ from 850–2000 based on regression of the 30-year binned values (Methods) (Fig. 1a). A positive relationship between GMST and δ_{precip} may be expected from high-latitude ice cores^{12,22,23}, but positive relationships in composite $\Delta^{18}\text{O}_{\delta_{\text{precip}}}$ persist even when such records are excluded (Extended Data Fig. 1) and also occur at mid and low latitudes, especially after 1850 (Extended Data Fig. 2). In addition to the composites, the positive relationship between δ_{precip} and GMST is evident in PC1 of the δ_{precip} records spanning the entire CE (Extended Data Fig. 3a,b) and in iCESM simulations (Fig. 3a,d; Extended Data Fig. 4). In iCESM, the regression slope between GMST and global, 30-year smoothed, mean annual $\delta^{18}\text{O}_{\text{precip}}$ from 850–2000 is $0.25\text{\textperthousand} ^\circ\text{C}^{-1}$ and $0.48\text{\textperthousand} ^\circ\text{C}^{-1}$ when calculated using

Iso2k site locations (which, for δ_{precip} records, excludes nearly all ocean grid cells and regions where site-level regression slopes are close to 0; Extended Data Fig. 4). The iCESM slopes are shallower than in the Iso2k data, but the global slope is consistent with earlier general circulation



model (GCM) estimates of $0.3\text{‰ }^{\circ}\text{C}^{-1}$ during the last deglaciation²⁴ and simplified model estimates of zonal-mean temporal slopes of $-0.1\text{--}0.4\text{‰ }^{\circ}\text{C}^{-1}$ for most latitudes²⁵. The discrepancy between the Iso2k and iCESM temporal slopes may reflect model biases in extra-tropical moisture transport and positive δ_{precip} biases at the high latitudes¹⁸. However, the global temporal slope between GMST and δ_{precip} has not been quantified observationally—unlike spatially derived slopes between site-level air temperature and δ_{precip} ^{11,12,22}—because modern δ_{precip} measurements in most regions are either absent or too short and discontinuous (most records <10 years) to do so beyond the scale of a few years^{26,27}. Despite differences in magnitude, both iCESM and Iso2k data demonstrate that a positive relationship between GMST and δ_{MW} is a persistent feature of the global water cycle for the CE. The 30-year binned Iso2k temporal slope of $0.68 \pm 0.20 \text{‰ }^{\circ}\text{C}^{-1}$ should be considered a benchmark to be tested as longer observations and reanalyses become available.

Ice core and marine sediment studies have long recognized the importance of air temperature in driving high-latitude δ_{MW} and of global ice volume in driving global δ_{SW} on glacial–interglacial timescales and across the Cenozoic^{12,23}. However, the nature of this relationship has remained uncertain on the shorter (decadal to centennial) timescales most relevant for understanding modern climate change and its impacts on water resources. Our results provide the first observational evidence that GMST drives temporal changes in δ_{MW} and δ_{SW} and therefore changes in the hydrological cycle on such timescales. Mechanisms other than global ice volume, which has not changed substantially during the CE, are therefore required to explain this relationship.

Although the Iso2k analyses are the first to document it, stable isotope theory and experimental studies provide ample foundation for a positive imprint of GMST on global δ_{MW} , which our spatially distributed (albeit not spatially continuous) proxy network approximates. At the global scale, a relationship between δ_{MW} and GMST will integrate all processes that relate local-scale δ_{MW} with GMST while balancing out regional distributions of heavy vs light isotopologues throughout the water cycle. Variations in global δ_{MW} therefore reflect variations in the isotopic composition of the global oceanic and atmospheric reservoirs. Atmospheric δ_{vapour} is ultimately governed by the isotopic composition of water evaporated from the oceans. Equilibrium fractionation is greater at lower temperatures^{12,28}, so in a cooler world, the liquid-to-vapour difference in $\delta^{18}\text{O}$ is higher than in warmer conditions (that is, lower δ_{vapour} in the saturated atmospheric layer above the ocean surface). Kinetic fractionation further decreases atmospheric δ_{vapour} as newly evaporated vapour diffuses and mixes into the undersaturated free atmosphere, with stronger fractionation when the lower troposphere is less humid^{29,30}. A globally cooler and drier troposphere should therefore decrease δ_{vapour} to a greater extent than a warmer and more humid troposphere. Global δ_{vapour} is further modified by temperature-dependent fractionation as precipitation forms and condensation preferentially removes ^{18}O and decreases δ_{vapour} , with greater isotopic discrimination at colder condensation temperatures^{12,28}.

iCESM simulations indicate multiple mechanisms play a role (Fig. 3). Higher GMST is associated with higher $\delta^{18}\text{O}$ of water vapour flux from evaporating seawater into the saturated boundary layer ($0.14\text{‰ }^{\circ}\text{C}^{-1}$), following the Craig–Gordon model^{13,31}, slightly higher relative humidity with respect to sea surface temperature ($0.77\text{‰ }^{\circ}\text{C}^{-1}$) (Methods) and ultimately, higher atmospheric $\delta^{18}\text{O}_{\text{vapour}}$ ($0.30\text{‰ }^{\circ}\text{C}^{-1}$). Global δ_{precip} therefore reflects not only the δ_{vapour} determined during ocean evaporation and mixing into the free atmosphere but also the subsequent depletion of ^{18}O in atmospheric vapour in the atmosphere through condensation, which via equilibrium fractionation is stronger in a cooler climate. Stronger depletion of heavy isotopes in precipitation also occurs with more vigorous circulation and shorter residence time of atmospheric moisture³². For precipitation integrated over the timescales of most proxy systems (weeks to months), δ_{precip} could become even lower when global precipitation

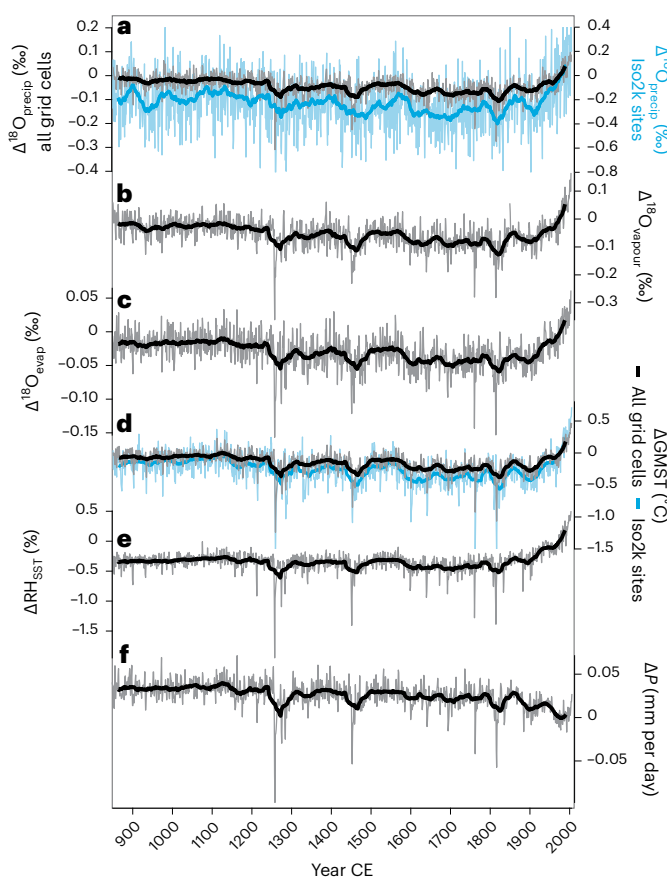


Fig. 3 | Global hydroclimate and isotopic anomalies in iCESM^{18–20}. **a**, Ensemble mean, amount-weighted mean annual $\Delta^{18}\text{O}_{\text{precip}}$ anomaly relative to 1961 to 1990 mean (thin grey line) and 30-year running mean (thick black line) for all grid cells and for only grid cells containing Iso2k site locations (blue lines). Note, right y axis in **a** is scaled 2× that of the left. **b–f**, As in **a**, but for global column-averaged $\Delta^{18}\text{O}_{\text{vapour}}$ (**b**), $\Delta^{18}\text{O}$ of evaporative flux from the global oceans (**c**), GMST (**d**), relative humidity over the low- and mid-latitude oceans (60°N – 60°S) with respect to saturation vapour pressure at sea surface temperature (RH_{sst})^{13,29,30} (**e**) and global precipitation rate (P) (**f**).

rates are high relative to the amount of precipitable water in the atmosphere and higher when atmospheric humidity increases to a greater extent than precipitation rate, as in the twentieth century (Fig. 3; ref. 33).

Theory and simplified model experiments suggest that a cooler global atmosphere could also favour stronger latitudinal gradients in δ_{precip} (ref. 12), as lower temperatures increase distillation along the water's path from the subtropics to the poles^{22,34}. A cooler atmosphere may also shift evaporative source regions equatorward, driving a greater fraction of high-latitude precipitation to be sourced remotely²⁵, which strongly affects δ_{precip} at those latitudes³⁵. The latitudinal gradient in Iso2k δ_{precip} records between 40° and 70°N and S is approximately -0.48‰ per degree latitude, in agreement with observed modern slopes of about -0.3‰ to -0.6‰ per degree latitude (refs. 22,34). However, we observe no difference in this gradient between the Little Ice Age and the twentieth century—the globally coldest and warmest intervals of the CE, respectively^{1,36} (Extended Data Fig. 5). Hence, either equator-to-pole Rayleigh distillation is counterbalanced by changes in spatial patterns of global evaporative recharge and moisture transport relative to precipitation^{25,35} or the spread in Iso2k δ_{precip} records is too large to resolve changing gradients during the LM when temperature changes are relatively small. As spatial gradients are averaged out at the global scale, further experiments with both simplified models and

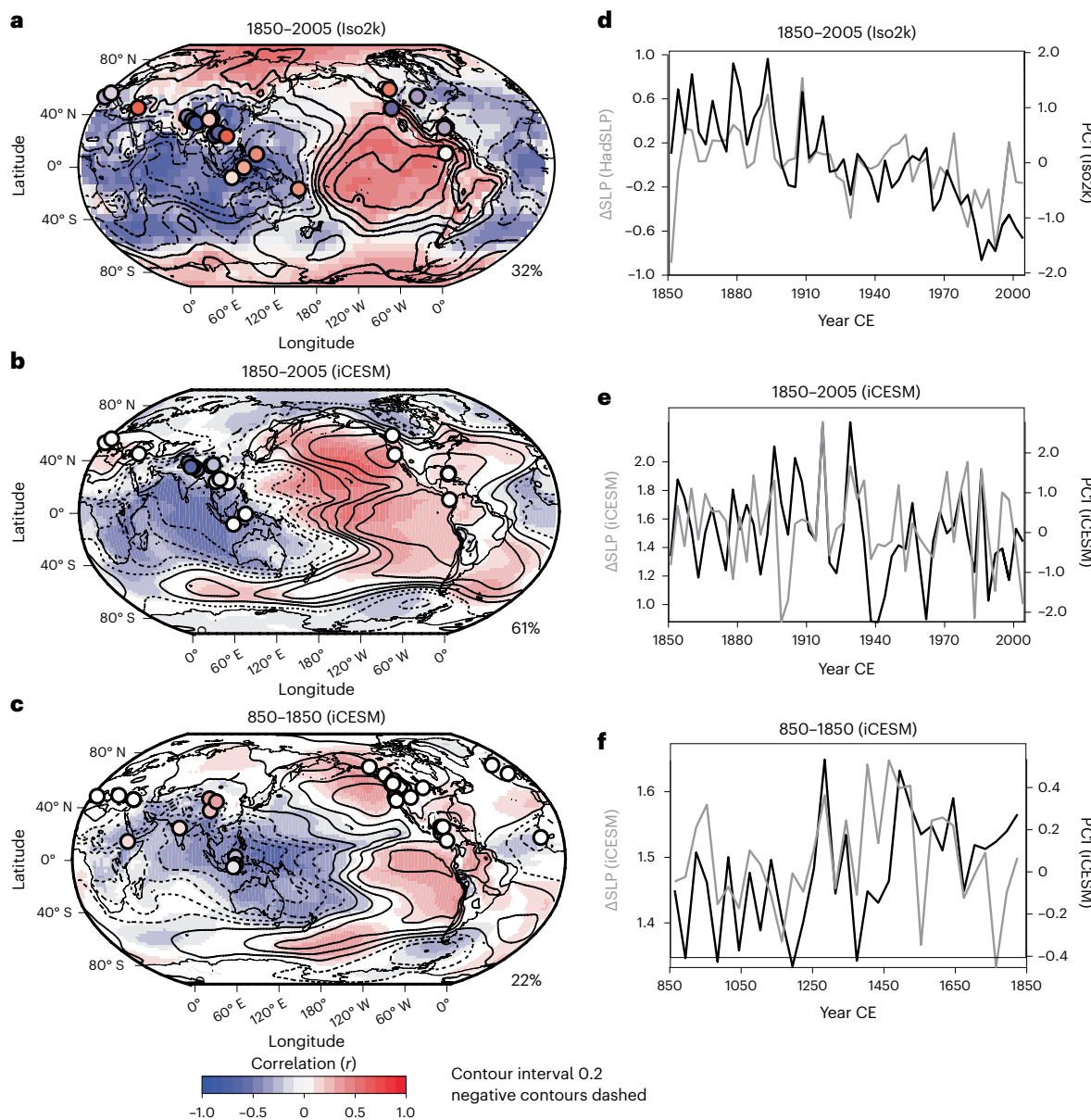


Fig. 4 | Isotopic fingerprint of the PWC in Iso2k and iCESM. **a**, Shading is the correlation between observed SLP and PC1 of three-year binned Iso2k EM records (1850 to 2005). Symbol colours denote site loading on PC1. Unfilled contours denote correlation between SLP and PWC index ΔSLP . **b**, Correlation between SLP and ensemble mean PC1 of three-year binned 0–10 cm $\delta^{18}\text{O}_{\text{soil}}$ in iCESM

experiments (1850 to 2005)^{18–20}, using grid cells of Iso2k¹⁵ EM sites (symbols). **c**, As in **b**, but for 30-year binned data from 850 to 1850. **d–f**, Time series of PC1 (black line) and ΔSLP (grey line) corresponding to panels **a–c**. Maps created in MATLAB using m_map for coastlines.

isotope-enabled GCMs are needed to quantitatively decompose the relative importance of ocean evaporation, condensation and global precipitation and evaporation patterns on the global-scale GMST– δ_{precip} relationship.

Patterns of regional variability

Despite its influence on global mean δ_{MW} , GMST explains neither the spatial patterns nor the shorter-term variability in δ_{MW} and δ_{SW} (Fig. 2 and Extended Data Fig. 6). Instead, site-level PC1 loadings, LM trends and centennial anomalies in the $\delta^{18}\text{O}$ of δ_{precip} -driven records and EM-driven records (hereafter, $\delta^{18}\text{O}_{\delta\text{precip}}$ and $\delta^{18}\text{O}_{\text{EM}}$, respectively) are spatially heterogeneous (Figs. 1 and 2 and Extended Data Figs. 7–9). Although non-climatic processes and noise probably contribute to this variability, this result also indicates that regional water balance, atmospheric circulation and precipitation characteristics dominate regional

δ_{MW} , not just in the late twentieth/early twenty-first centuries^{26,27} but also on multi-decadal to millennium-long timescales. In the Arctic and the tropical Andes, negative trends in the $\delta^{18}\text{O}$ of δ_{precip} -Sensitive records (hereafter, $\delta^{18}\text{O}_{\delta\text{precip}}$) and positive PC1 loadings agree with documented Little Ice Age climate changes: high-latitude cooling, which lowered δ_{precip} in the Arctic³⁷, and intensification of the South American summer monsoon, which lowered δ_{precip} in the Andes³⁸. In eastern China and the maritime continent, positive PC1 loadings and negative trends in $\delta^{18}\text{O}_{\delta\text{precip}}$ and $\delta^{18}\text{O}_{\text{EM}}$ over the LM indicate increasing effective moisture, with depletion of heavy isotopes at some sites enhanced by intensifying convection and moisture transport within the East Asian and Australasian summer monsoons^{39,40}. In northwestern North America and Central America, negative PC1 loadings and positive trends in $\delta^{18}\text{O}_{\delta\text{precip}}$ and $\delta^{18}\text{O}_{\text{EM}}$ indicate increasing $\delta^{18}\text{O}_{\text{MW}}$ and declining EM over the LM, while southwestern North America shows the opposite pattern,

consistent with other LM proxy reconstructions^{41,42}. $\delta^{18}\text{O}_{\text{EM}}$ from lakes exhibit the clearest trends in western North America, probably because δ_{precip} in the western North American interior is especially sensitive to changes in water balance²⁷ and enhanced evaporation during dry periods then amplifies increases in lake water $\delta^{18}\text{O}$. This explains why coherent patterns emerge in western North American isotopic proxy records despite substantial heterogeneity in compilations that blend isotopic and non-isotopic records⁴².

Opposing precipitation anomalies between southwestern North America and Central Asia versus the Maritime Continent and South Asia during the LM have previously been attributed to variability in the El Niño/Southern Oscillation⁴³, the interannual component of the east–west atmospheric overturning circulation over the tropical Pacific known as the Pacific Walker Circulation (PWC)⁴⁴. An underlying influence of the PWC may also explain some of the regional coherency in Iso2k δ_{MW} (ref. 45). In modern precipitation, strengthening and weakening of the PWC drives opposing precipitation and $\delta^{18}\text{O}_{\text{precip}}$ anomalies in Asia and the Americas due to changes in precipitation amount, moisture source and transport pathways²⁶. For example, rerouting of the jet stream during El Niño events alters Pacific Ocean moisture trajectories towards southwestern rather than northwestern North America^{46,47}. To the extent that these relationships persist beyond interannual timescales, changes in moisture transport and EM provide a plausible mechanism for multi-decadal to centennial patterns in Asian and western North American $\delta^{18}\text{O}_{\text{EM}}$.

Evidence for the PWC's influence on Iso2k records is stronger on sub-decadal timescales during the historical period (1850–2005), when instrumental observations are available for direct comparison. We correlated PC1 of three-year binned Iso2k EM records with observed sea-level pressure (SLP) and found that the associated pattern mimics the observed global expression of the PWC (Fig. 4a). Similarly, in iCESM experiments, PC1 of soil water $\delta^{18}\text{O}$ ($\delta^{18}\text{O}_{\text{soil}}$) at Iso2k EM sites displays an SLP pattern that resembles iCESM's PWC (Fig. 4b). There is vigorous debate surrounding the extent to which the PWC fluctuates on multi-decadal and longer timescales, either due to internal variability in the climate system or to external forcing^{45,48–50}. Our results suggest that the PWC was the predominant influence on interannual $\delta^{18}\text{O}_{\text{precip}}$ not only from 1982 to 2015²⁶, but at least since 1850, and probably on multi-decadal timescales before 1850.

Our results reveal a remarkably consistent relationship between GMST and δ_{MW} throughout the CE, despite relatively constant ice–ocean boundary conditions. Between 1850 and 2000, global δ_{precip} increased by at least 0.56‰, indicative of a warmer, more humid troposphere. Global δ_{MW} and regional δ_{MW} appear to adjust to changing temperature and atmospheric circulation patterns, respectively, within decades—similar to the timescale of the forcing itself. Expansion of δ_{MW} observational networks will be critical for detecting and attributing shifts in rainfall, drought and circulation as the planet continues to warm.

Online content

Any methods, additional references, Nature Portfolio reporting summaries, source data, extended data, supplementary information, acknowledgements, peer review information; details of author contributions and competing interests; and statements of data and code availability are available at <https://doi.org/10.1038/s41561-023-01291-3>.

References

- PAGES 2k Consortium. Consistent multidecadal variability in global temperature reconstructions and simulations over the Common Era. *Nat. Geosci.* **12**, 643–649 (2019).
- PAGES 2k Consortium. A global multiproxy database for temperature reconstructions of the Common Era. *Sci. Data* **4**, 170088 (2017).
- IPCC Climate Change 2014: Impacts, Adaptation, and Vulnerability (eds Field, C. B. et al.) (Cambridge Univ. Press, 2014).
- PAGES Hydro2k Consortium. Comparing proxy and model estimates of hydroclimate variability and change over the Common Era. *Clim. Past* **13**, 1851–1900 (2017).
- Rozanski, K. in *Isotopes in the Water Cycle* (eds Aggarwal, P. K. et al.) 291–302 (Springer, 2005).
- Galewsky, J. et al. Stable isotopes in atmospheric water vapor and applications to the hydrologic cycle. *Rev. Geophys.* **54**, 809–865 (2016).
- Konecky, B. L., Noone, D. C. & Cobb, K. M. The influence of competing hydroclimate processes on stable isotope ratios in tropical rainfall. *Geophys. Res. Lett.* **46**, 1622–1633 (2019).
- Jasechko, S. Global isotope hydrogeology—review. *Rev. Geophys.* **57**, 835–965 (2019).
- Sturm, C., Zhang, Q. & Noone, D. An introduction to stable water isotopes in climate models: benefits of forward proxy modelling for paleoclimatology. *Clim. Past* **6**, 115–129 (2010).
- Gat, J. *Isotope Hydrology: A Study of the Water Cycle* 6 (Imperial College Press, 2010).
- Bowen, G. J., Cai, Z., Fiorella, R. P. & Putman, A. L. Isotopes in the water cycle: regional- to global-scale patterns and applications. *Annu. Rev. Earth Planet. Sci.* **47**, 453–479 (2019).
- Dansgaard, W. Stable isotopes in precipitation. *Tellus* **16**, 436–468 (1964).
- Craig, H. & Gordon, L. I. in *Stable Isotopes in Oceanographic Studies and Paleotemperatures* (ed. Tongiorgi, E.) 9–130 (Consiglio Nazionale Delle Ricerche, Laboratorio di Geologia Nucleare-Pisa, 1965).
- Rohling, E. J. in *Encyclopedia of Quaternary Science* 2nd edn (eds. Elias, S. A. & Mock, C. J.) 915–922 (Elsevier, 2013).
- Konecky, B. L. et al. The Iso2k database: a global compilation of paleo- $\delta^{18}\text{O}$ and $\delta^2\text{H}$ records to aid understanding of Common Era climate. *Earth Syst. Sci. Data* **12**, 2261–2288 (2020).
- Urey, H. C. Oxygen isotopes in nature and in the laboratory. *Science* **108**, 489–496 (1948).
- Kaufman, D. et al. Holocene global mean surface temperature, a multi-method reconstruction approach. *Sci. Data* **7**, 201 (2020).
- Brady, E. et al. The connected isotopic water cycle in the Community Earth System Model Version 1. *J. Adv. Model. Earth Syst.* **11**, 2547–2566 (2019).
- Stevenson, S. et al. Volcanic eruption signatures in the isotope-enabled last millennium ensemble. *Paleoceanogr. Paleoclimatol.* **34**, 1534–1552 (2019).
- Otto-Bliesner, B. L. et al. Climate variability and change since 850 CE: an ensemble approach with the Community Earth System Model. *Bull. Am. Meteorol. Soc.* **97**, 735–754 (2016).
- Thompson, D. M. et al. Identifying hydro-sensitive coral $\delta^{18}\text{O}$ records for improved high-resolution temperature and salinity reconstructions. *Geophys. Res. Lett.* **49**, e2021GL096153 (2022).
- Rozanski, K., Araguás-Araguás, L. & Gonfiantini, R. in *Climate Change in Continental Isotopic Records* (eds Stewart, P. K. et al.) 1–36 (American Geophysical Union, 1993).
- Petit, J. R. et al. Climate and atmospheric history of the past 420,000 years from the Vostok ice core, Antarctica. *Nature* **399**, 429–436 (1999).
- Guan, J. et al. Understanding the temporal slope of the temperature–water isotope relation during the deglaciation using isoCAM3: the slope equation. *J. Geophys. Res.* **121**, 10,342–10,354 (2016).
- Siler, N. et al. The large-scale, long-term coupling of temperature, hydrology, and water isotopes. *J. Clim.* **34**, 6725–6742 (2021).
- Falster, G., Konecky, B., Madhavan, M., Stevenson, S. & Coats, S. Imprint of the Pacific Walker Circulation in global precipitation $\delta^{18}\text{O}$. *J. Clim.* **34**, 8579–8597 (2021).

27. Putman, A. L., Bowen, G. J. & Strong, C. Local and regional modes of hydroclimatic change expressed in modern multidecadal precipitation oxygen isotope trends. *Geophys. Res. Lett.* **48**, e2020GL092006 (2021).
28. Majoube, M. Fractionnement en oxygène 18 et en deutérium entre l'eau et sa vapeur. *J. Chim. Phys.* **68**, 1423–1436 (1971).
29. Craig, H., Gordon, L. I. & Horibe, Y. Isotopic exchange effects in the evaporation of water: 1. low-temperature experimental results. *J. Geophys. Res. C* **68**, 5079–5087 (1963).
30. Horita, J., Rozanski, K. & Cohen, S. Isotope effects in the evaporation of water: a status report of the Craig–Gordon model. *Isotopes Environ. Health Stud.* **44**, 23–49 (2008).
31. Nusbaumer, J., Wong, T. E., Bardeen, C. & Noone, D. Evaluating hydrological processes in the Community Atmosphere Model Version 5 (CAM5) using stable isotope ratios of water. *J. Adv. Model. Earth Syst.* **9**, 949–977 (2017).
32. Aggarwal, P. K. et al. Stable isotopes in global precipitation: a unified interpretation based on atmospheric moisture residence time. *Geophys. Res. Lett.* **39**, L11705 (2012).
33. Held, I. M. & Soden, B. J. Robust responses of the hydrological cycle to global warming. *J. Clim.* **19**, 5686–5699 (2006).
34. Gat, J. R., Mook, W. G. & Meijer, H. A. *Environmental Isotopes in the Hydrological Cycle* 2nd edn (International Atomic Energy Agency, 2001).
35. Bailey, A., Posmentier, E. & Feng, X. Patterns of evaporation and precipitation drive global isotopic changes in atmospheric moisture. *Geophys. Res. Lett.* **45**, 7093–7101 (2018).
36. Neukom, R., Steiger, N., Gómez-Navarro, J. J., Wang, J. & Werner, J. P. No evidence for globally coherent warm and cold periods over the preindustrial Common Era. *Nature* **571**, 550–554 (2019).
37. Stuiver, M., Grootes, P. M. & Braziunas, T. F. The GISP2 $\delta^{18}\text{O}$ climate record of the past 16,500 years and the role of the sun, ocean, and volcanoes. *Quat. Res.* **44**, 341–354 (1995).
38. Vuille, M. et al. A review of the South American monsoon history as recorded in stable isotopic proxies over the past two millennia. *Clim. Past* **8**, 1309–1321 (2012).
39. Zhao, K. et al. A high-resolved record of the Asian summer monsoon from Dongge Cave, China for the past 1,200 years. *Quat. Sci. Rev.* **122**, 250–257 (2015).
40. Konecky, B. L. et al. Intensification of southwestern Indonesian rainfall over the past millennium. *Geophys. Res. Lett.* **40**, 386–391 (2013).
41. Cook, E. R., Seager, R., Cane, M. A. & Stahle, D. W. North American drought: reconstructions, causes, and consequences. *Earth Sci. Rev.* **81**, 93–134 (2007).
42. Shuman, B. N. et al. Placing the Common Era in a Holocene context: millennial to centennial patterns and trends in the hydroclimate of North America over the past 2,000 years. *Clim. Past* **14**, 665–686 (2018).
43. Li, J., Xie, S.-P. & Cook, E. R. El Niño phases embedded in Asian and North American drought reconstructions. *Quat. Sci. Rev.* **85**, 20–34 (2014).
44. Bjerknes, J. Atmospheric teleconnections from the equatorial Pacific. *Mon. Weather Rev.* **97**, 163–172 (1969).
45. Falster, G., Konecky, B., Coats, S. & Stevenson, S. Forced changes in the Pacific Walker circulation over the past millennium. *Nature* **622**, 93–100 (2023).
46. Kong, W. & Chiang, J. C. H. Southward shift of westerlies intensifies the east Asian early summer rainband following El Niño. *Geophys. Res. Lett.* **47**, e2020GL088631 (2020).
47. Seager, R. et al. Adjustment of the atmospheric circulation to tropical Pacific SST anomalies: variability of transient eddy propagation in the Pacific–North America sector. *Q. J. R. Meteorolog. Soc.* **136**, 277–296 (2010).
48. Wittenberg, A. T. Are historical records sufficient to constrain ENSO simulations? *Geophys. Res. Lett.* **36**, L12702 (2009).
49. Collins, M. et al. The impact of global warming on the tropical Pacific Ocean and El Niño. *Nat. Geosci.* **3**, 391–397 (2010).
50. Vecchi, G. et al. Weakening of tropical Pacific atmospheric circulation due to anthropogenic forcing. *Nature* **441**, 73–76 (2006).

Publisher's note Springer Nature remains neutral with regard to jurisdictional claims in published maps and institutional affiliations.

Springer Nature or its licensor (e.g. a society or other partner) holds exclusive rights to this article under a publishing agreement with the author(s) or other rightsholder(s); author self-archiving of the accepted manuscript version of this article is solely governed by the terms of such publishing agreement and applicable law.

© The Author(s), under exclusive licence to Springer Nature Limited 2023

¹Department of Earth, Environmental, and Planetary Sciences, Washington University, Saint Louis, MO, USA. ²School of Earth and Sustainability, Northern Arizona University, Flagstaff, AZ, USA. ³Research School of Earth Sciences and ARC Centre of Excellence for Climate Extremes, Australian National University, Canberra, Australian Capital Territory, Australia. ⁴Bren School of Environmental Science and Management, University of California, Santa Barbara, CA, USA. ⁵NST Environment, ANSTO, Sydney, New South Wales, Australia. ⁶Department of Earth, Ocean, and Atmospheric Science, Florida State University, Tallahassee, FL, USA. ⁷Department of Geosciences, University of Arizona, Tucson, AZ, USA. ⁸School of Geography, University of Nottingham, Nottingham, UK. ⁹School of Physics, Chemistry and Earth Sciences, The University of Adelaide, Adelaide, South Australia, Australia. ¹⁰Department of Geography and Anthropology, Coastal Studies Institute, Louisiana State University, Baton Rouge, LA, USA. ¹¹Department of Environmental Chemistry, Institute of Environmental Assessment and Water Research (IDAEA-CSIC), Barcelona, Spain. ¹²Department of Geology, University at Buffalo, Buffalo, NY, USA.

¹³Department of Geology, Department of Plant Biology, University of Illinois at Urbana-Champaign, Urbana, IL, USA. ¹⁴Department of Earth, Environmental, and Planetary Sciences, Rice University, Houston, TX, USA. ¹⁵MARUM Center for Marine Environmental Sciences, Bremen University, Bremen, Germany.

¹⁶Institute of Ecology and Geography, Siberian Federal University, Krasnoyarsk, Russian Federation. ¹⁷Department of Forest Dynamics, Swiss Federal Institute for Forest, Snow and Landscape Research WSL, Birmensdorf, Switzerland. ¹⁸Institute for Geological and Geochemical Research, Research Centre for Astronomy and Earth Sciences, Eötvös Loránd Research Network, Budapest, Hungary. ¹⁹CSFK, MTA Centre of Excellence, Budapest, Hungary.

²⁰Polar Terrestrial Environmental Systems, Alfred Wegener Institute Helmholtz Centre for Polar and Marine Research, Potsdam, Germany. ²¹Department of Geography, Geomatics and Environment, University of Toronto–Mississauga, Mississauga, Ontario, Canada. ²²School of Earth and Atmospheric Science, Georgia Institute of Technology, Atlanta, GA, USA. ²³West Australian Biogeochemistry Centre, School of Biological Sciences, The University of Western Australia, Perth, Western Australia, Australia. *A list of authors and their affiliations appears at the end of the paper. ✉e-mail: bkonecky@wustl.edu

Iso2k Project Members

Bronwen L. Konecky¹, Nicholas P. McKay², Georgina M. Falster^{1,3}, Samantha L. Stevenson⁴, Matt J. Fischer⁵, Alyssa R. Atwood⁶, Diane M. Thompson⁷, Matthew D. Jones⁸, Jonathan J. Tyler⁹, Kristine L. DeLong¹⁰, Belen Martrat¹¹, Elizabeth K. Thomas¹², Jessica L. Conroy¹³, Sylvia G. Dee¹⁴, Lukas Jonkers¹⁵, Olga V. Churakova (Sidorova)^{16,17}, Zoltán Kern^{18,19}, Thomas Opel²⁰, Trevor J. Porter²¹, Hussein R. Sayani²², Grzegorz Skrzypek²³, Nerilie J. Abram^{3,24}, Kerstin Braun²⁵, Matthieu Carré²⁶, Olivier Cartapanis²⁷, Laia Comas-Bru²⁸, Mark A. Curran²⁹, Emilie P. Dassié³⁰, Michael Deininger³¹, Dmitry V. Divine³², Alessandro Incarbona³³, Darrell S. Kaufman², Nikita Kaushal³⁴, Robert M. Klaebe³⁵, Hannah R. Kulus², Guillaume Leduc³⁶, Shreyas R. Managave³⁷, P. Graham Mortyn³⁸, Andrew D. Moy²⁹, Anais J. Orsi^{39,40}, Judson W. Partin⁴¹, Heidi A. Roop⁴², Marie-Alexandrine Sicre⁴³, Lucien von Gunten⁴⁴ & Kei Yoshimura⁴⁵

²⁴Australian Centre for Excellence in Antarctic Science, Australian National University, Canberra, Australian Capital Territory, Australia. ²⁵Arizona State University, Tempe, AZ, USA. ²⁶LOCEAN, Sorbonne Universités (UPMC)-CNRS-IRD-MNHN, Paris, France. ²⁷CEREGE, Aix Marseille Université, CNRS, IRD, INRAE, Aix-en-Provence, France. ²⁸University of Reading, Reading, UK. ²⁹Australian Antarctic Division, Kingston, Tasmania, Australia. ³⁰University of Bordeaux, Bordeaux, France. ³¹Johannes Gutenberg University Mainz, Mainz, Germany. ³²Norwegian Polar Institute, Tromsø, Norway. ³³Palermo University, Palermo, Italy. ³⁴University of Oxford, Oxford, UK. ³⁵The University of Adelaide, Adelaide, South Australia, Australia. ³⁶Aix Marseille University, CNRS, IRD, INRAE, Coll France, CEREGE, Aix-en-Provence, France. ³⁷Indian Institute of Science Education and Research, Pune, India. ³⁸Universitat Autònoma de Barcelona (UAB), Barcelona, Spain. ³⁹Laboratoire de Sciences du Climat et de l'Environnement, LSCE-IPSL, CEA, CNRS, UVSQ, UMR8212, Université Paris-Saclay, Gif-sur-Yvette, France. ⁴⁰Department of Earth, Ocean and Atmospheric Sciences, The University of British Columbia, Vancouver, British Columbia, Canada. ⁴¹University of Texas at Austin, Austin, TX, USA. ⁴²University of Minnesota, Minneapolis, MN, USA. ⁴³CNRS and Sorbonne Université, Paris, France. ⁴⁴PAGES International Project Office, Bern, Switzerland. ⁴⁵The University of Tokyo, Tokyo, Japan.

Methods

Disaggregation of analyses by isotope interpretation

All global analyses presented in this paper were disaggregated by isotope interpretation rather than by the original authors' climatic interpretation. This approach avoids building into our synthesis a priori assumptions about the specific climatic variable driving $\delta^{18}\text{O}$ and $\delta^2\text{H}$ variability in each record, the basis for which is not always explained in the original publications. In addition, many records contain multiple climatic interpretations (for example, speleothem $\delta^{18}\text{O}$ being driven mainly by monsoonal rainfall amount but amplified by the ratio of summer vs winter moisture source changes^{51–53}), and the relative importance of each variable was impossible to objectively evaluate for every timescale, region and proxy system in the database. Finally, climatic interpretations of isotope-based proxy records are continually evolving as new information emerges from environmental monitoring and modelling studies (for example, moisture source and transport characteristics driving Greenland ice core $\delta^{18}\text{O}$ variability^{25,35,54–56}, seawater $\delta^{18}\text{O}$ driving coral $\delta^{18}\text{O}$ in some regions²¹). The isotope interpretation groupings are less subject to interpretation because they chiefly represent isotope systematics and the physical pools of environmental waters that each proxy sensor imbibes.

We separated δ_{precip} and EM records because EM proxies integrate information about evaporation that is not expected from pure δ_{precip} proxies, which are mainly driven by factors influencing condensation (for example, air temperature, degree of rainout, import of moisture from different sources)^{7,11}.

Calculation of composites

All records were extracted from the PAGES Iso2k Database v 1.0.0 (refs. 15,57). The database contains metadata on the principal determinants of isotopic composition in the measured material (for example, the $\delta^{18}\text{O}$ of precipitation that forms glacial ice or cave dripwaters) and the record's climatic interpretation (for example, atmospheric temperature at condensation level, rainout due to monsoon intensity), as interpreted by the original studies' authors and our team of archive experts¹⁵. For each isotope interpretation group, we calculated an ensemble of 100 composite $\delta^{18}\text{O}$ time series for the CE. Before calculation, we filtered the database to only include the 'primary' time series for each site and then grouped records according to the primary driver of isotopic variability, that is, EM, temperature or δ_{precip} (refs. 15,57) (entitled 'EffectiveMoisture', 'Temperature' and 'P_isotope' in the 'isotopeInterpretation1_variableGroup' metadata field of the Iso2k database).

For records with isotope interpretation 'P_isotope', we also calculated separate composites for (1) glacier ice only and (2) excluding glacier ice (Extended Data Fig. 1). This separation was performed to assess whether composite $\Delta^{18}\text{O}_{\text{precip}}$ is overprinted by the large number of ice core records from high latitudes and high elevations, where temperature-driven isotopic fractionation may disproportionately affect δ_{MW} (ref. 2). An especially strong temperature– δ_{MW} relationship may be unsurprising in the glacier ice $\delta^{18}\text{O}$ system. Glacier ice reflects δ_{precip} more directly than other proxy sensors, which reflect pools of meteoric water (for example, soil water and lake water) that are influenced by precipitation and other secondary processes such as evaporation or aquifer mixing. Glacier ice is found at high latitudes and altitudes, where cold temperatures drive stronger stable isotope fractionation due to Rayleigh distillation and global patterns of precipitation vs evaporative recharge^{10–12,22,23,25,35,55}. Most of the glacier ice records included in the Iso2k database are consistently interpreted as temperature indicators and were included in the PAGES 2k (refs. 1,2) temperature database used for GMST calculations.

Despite these considerations, the observed global δ_{MW} –temperature relationship persists even when glacier ice records are removed from the δ_{precip} composite (Extended Data Fig. 1) and in low- and mid-latitudes where local temperature effects on δ_{precip} are small¹²

(Fig. 2). The overall patterns in PC1 are also similar regardless of whether glacier ice records are included or excluded (Extended Data Figs. 3 and 8). Therefore, the inclusion or exclusion of glacier ice records does not substantially affect the composites or PCA, supporting that the strong temperature– δ_{MW} relationship in our data is due to the overall influence of temperature on the global pool of meteoric water and not due to the strong effect of air temperature on high-latitude ice cores.

Records with ten or fewer data values within the CE were excluded from the analysis. $\delta^2\text{H}$ records ($n = 45$ in composite $\Delta^{18}\text{O}_{\text{precip}}$, $n = 12$ in composite $\Delta^{18}\text{O}_{\text{EM}}$) were divided by eight to scale the magnitude of their variance with that of $\delta^{18}\text{O}$ in global meteoric waters⁵⁸. This was done to avoid erroneously high apparent climate variability at $\delta^2\text{H}$ sites simply from the eight-times-higher variability in $\delta^2\text{H}$ relative to $\delta^{18}\text{O}$, which arises from relative differences in equilibrium fractionation factors between liquid and vapour for these isotope ratios⁵⁸. Local slopes were not available for the 12 records from evaporative water bodies in composite $\Delta^{18}\text{O}_{\text{EM}}$, so the global scaling of 8 was used.

Records in the Iso2k database have a wide variety of temporal resolution, length and coverage over the CE¹⁵. To align records to a common interval and resolution, the data were averaged into equal bins of 30 years spanning the CE, which approximates the average resolution of the lower resolution archive types in the database (marine and lake sediments). Records contributing to each bin were mean centred but not scaled by variance, as described below. To minimize aliasing, the data were binned following a modified nearest-neighbour annual interpolation procedure¹⁷. This approach accounts for the fact that for the non-annually resolved data, the age of a sample at a given depth typically represents more than one year of accumulation (and up to several years or decades or even longer for some low-resolution sedimentary records) and may therefore contain climate information that is relevant to more than one bin. The duration of each sample is not consistently recorded in the Iso2k database (or the primary references), so to estimate sample coverage we calculated the distribution of gaps between adjacent observations in each time series, and used nearest-neighbour interpolation to estimate sample values spanning the intervals that are less than the 75th quantile of the distribution of all gaps between adjacent observations (consistent with Kaufman et al.¹⁷). Consequently, samples with resolution <30 years can potentially contribute to the weighted $\delta^{18}\text{O}$ calculation for up to two bins, though with less weight given to samples further from their published age. In the case of records with resolution >30 years, this data-spreading step allows observations to impact the composites across multiple bins, consistent with their interpretation as multi-decadal averages.

Record lengths also vary widely in the database, so there is no universal time period of common overlap within the CE. We therefore aligned the records using the Dynamic Compositing approach¹⁷, which uses randomly selected portions of each time series to adjust the $\delta^{18}\text{O}$ variance, then iteratively adjusts the mean $\delta^{18}\text{O}$ of each time series so that the mean of each record is minimally offset from all other records in the composite. This process was repeated for each of 100 ensemble members. Because the mean value of the records is adjusted during compositing, the composite values are now in relative $\Delta^{18}\text{O}$ (in %), rather than in their original $\delta^{18}\text{O}$ (or pre-scaled $\delta^2\text{H}$) values on the VSMOW-SLAP scale (that is, in $1,000 \times \delta$ notation where 0% refers to standard mean ocean water). Therefore, for convenience, composite $\Delta^{18}\text{O}$ was slightly shifted such that the mean of the ensemble median is 0%. The final composite $\Delta^{18}\text{O}$ values (Fig. 1) are therefore in units of % anomalies relative to the 2,000-year mean. Dynamic compositing was used in ref. 17 to produce calibrated reconstructions of palaeotemperature. Unlike surface air temperature observations, long and complete time series of globally distributed δ_{precip} , δ_{MW} and δ_{SW} observations are insufficient (for example, for δ_{precip} , large spatial coverage gaps and few records longer than ten years²⁶), and so calibrated reconstructions are not possible until these observational networks are improved.

PCA of Iso2k data

We used PCA to calculate empirical orthogonal functions (EOFs) from a subset of records in the Iso2k database that met requirements for temporal coverage (described below; Fig. 2). Before calculating the EOFs, we filtered the database as described for the $\Delta^{18}\text{O}$ composites and binned the raw data. PCA was performed using records in each of the three ‘isotope interpretation’ categories; for ‘P_isotope’ records, we performed separate PCA for (1) glacier ice and (2) ‘not glacier ice’ (that is, all P_isotope records that are not from glacier ice). PCA was performed on three temporal subsets: 0–1980 CE (30-year bins), 850–1840 (30-year bins) and 1850–2005 (three-year bins). Here we describe the methodology for the 850–1840 PCA that is shown in the main text, then outline any adaptations that were made for the other two intervals.

Before PCA, all records were truncated to a fixed time interval of 850–1840. Other time windows were explored and are presented in Extended Data Figs. 3 and 8. The 850–1840 interval was chosen to focus on pre-industrial variability, to avoid issues with records or chronologies not extending fully to either the present day or the start of the CE and to provide comparison with LM model experiments from 850–1850. (Note a 990-year interval was used because it is divisible by the 30-year bin size). Results of PCA on the 0–1980 interval (with 30-year bins) and 1850–2005 (with three-year bins) are shown in Extended Data Figs. 3 and 8. All data processing for these intervals was as below.

Records included in the PCA had to meet stricter time coverage and completeness requirements than records included in the composites. Binned records with <85% temporal coverage during the 850–1840 interval were excluded. EOF analysis was carried out on the matrix of remaining, screened time series using the Data Interpolation Empirical Orthogonal Function (DINEOF) method, which accounts for records with a small number of missing data points^{59,60}. DINEOF performs best when missing values are scattered randomly throughout the input data time series. In the case of Iso2k records, missing data are generally concentrated at the ends of records, and hence records with a large proportion of missing data have a large impact on the PC loadings (though less impact on the overall PC time series). To check for obvious artefacts induced by the data processing, we visually compared the binned and interpolated records with their raw data equivalents. We performed the PCA on the binned and interpolated data matrix using the `rda()` function of the ‘vegan’ package in R⁶¹. We scaled the interpolated records to unit variance because they are from different proxy systems and hence the raw data have widely ranging variance.

To test whether variability explained by the principal components could be explained stochastically, we tested the magnitude of the eigenvalues against a stochastic null hypothesis, using a block bootstrap method that accounts for decadal persistence (Extended Data Fig. 9). For the 850–1840 analysis, we split all raw data records that contributed to the EOF into ten-year blocks; we chose ten years because this separates interannual variance from interdecadal persistence. For each time series, we randomly selected an initial block, identified all blocks with similar means and randomly sampled one block from these. The next selected block was the successor to that randomly sampled block. Blocks with similar means were identified using nearest-neighbour-based ranking. For blocks with no successor (that is, where there is a gap in the time series), the successor block was randomly selected from all other blocks. The process was then repeated 1,000 times to produce an ensemble of time series. This method of re-sampling preserves the effects of (1) irregular time spacing, (2) the autocorrelation function (to lags >30 years) and (3) the time series processing steps (for example, binning) on the correlation structure of the raw (unprocessed) time series. We followed exactly the same steps for the 0–1980 PCA, using a 30-year bin size.

The 1850–2004 PCA was performed using three-year bins, on records with 80% coverage. Block bootstrap was performed using three-year blocks because 10-year blocks were too coarse for this short

time period. As with the above, records were binned and standardized but not detrended.

PCA with iCESM experiments

To compare the iCESM with Iso2k results, we performed PCA of 30-year binned iCESM surface soil water $\delta^{18}\text{O}$ ($\delta^{18}\text{O}_{\text{soil}}$), that is, the model variable most comparable to evaporation-sensitive systems such as lakes. We used data from Iso2k EM site locations, spanning 850–1850 and then regressed the ensemble mean first PC against model SLP. The binned $\delta^{18}\text{O}_{\text{soil}}$ was calculated for gridpoint time series corresponding to the ‘effective moisture’ sites, taken from each isotope-enabled Last Millennium Ensemble full-forcing ensemble member from the upper 0–10 cm of the soil profile in iCLM, then averaged to produce an ensemble mean. The upper 10 cm were chosen because in the model, isotopic fractionation is clearest at this level whereas $\delta^{18}\text{O}_{\text{soil}}$ of deeper soil layers rapidly approaches $\delta^{18}\text{O}_{\text{precip}}$ (refs. 18,62). EOF analysis was performed using $\delta^{18}\text{O}_{\text{soil}}$ because the ‘lake’ land cover type in iCLM4 is non-fractionating^{18,62} and hence no model variable is available for direct comparison with the large number of lake-based Iso2k $\delta^{18}\text{O}_{\text{EM}}$ proxies. Yet to first order, $\delta^{18}\text{O}_{\text{soil}}$ is similarly controlled by both $\delta^{18}\text{O}_{\text{precip}}$ and surface evaporation, and $\delta^{18}\text{O}_{\text{soil}}$ is also an adequate comparison to tree cellulose and speleothem records in the Iso2k EM category.

Correlations with sea-level pressure and calculation

of PWC index

Observed SLP and ΔSLP for the correlations against Iso2k HP PC1 (Fig. 4) were taken from the HadSLP2r dataset⁶³. Following the treatment of the Iso2k data, the HadSLP dataset was binned to three years but not detrended or deseasonalized (Fig. 4).

The index for the trans-Pacific SLP gradient (ΔSLP) is defined as anomalies (from the monthly climatology) in the difference between area-mean SLP over the central-eastern Pacific Ocean (160° W–180° W, 5° S–5° N) and the western Pacific and eastern Indian oceans (80° E–160° E, 5° S–5° N) (ref. 50). Positive ΔSLP values represent an increased zonal pressure gradient and hence stronger PWC (and vice versa). ΔSLP was calculated using HadSLP2r for comparisons with Iso2k (Fig. 4).

Magnitudes of change in Iso2k composites and in GMST

To estimate the magnitude of change in the three composite $\Delta^{18}\text{O}$ time series, we subtracted the composite $\Delta^{18}\text{O}$ value at 1000 CE from the composite $\Delta^{18}\text{O}$ value at 1850 CE for all 100 composite ensemble members. We likewise calculated the difference between 2000 CE and 1850 CE. Similarly for estimating the change in GMST during this interval, we subtracted the temperature anomaly at 1000 (1850) from the same at 1850 (2000) for all 7,000 ensemble members. In all cases, we report the mean and standard deviation of the distributions of magnitudes of change.

Calculation of isotope–temperature relationships in Iso2k data and iCESM experiments

We calculated the relationship between composite $\Delta^{18}\text{O}_{\text{precip}}$ (that is, an approximation of anomalies in the global mean $\delta^{18}\text{O}$ of precipitation, given the spatial distribution of 305 δ_{precip} -sensitive proxy records) and GMST between 850 and 2000. We binned all ensemble members from the most recent reconstruction of CE GMST¹ to match the $\Delta^{18}\text{O}_{\text{precip}}$ composite. We then calculated linear regressions for 10,000 unique combinations of composite $\Delta^{18}\text{O}_{\text{precip}}$ ensemble members ($n = 100$) on GMST ensemble member ($n = 7,000$) for the two time intervals. We report the mean and standard deviation of the distribution of regression coefficients for the two time intervals.

For iCESM, isotope/temperature relationships were calculated for 850–2000 (the period of overlap with Iso2k composites) using area-weighted, globally averaged, mean annual surface temperature and area-weighted, amount-weighted, mean annual global average

$\delta^{18}\text{O}_{\text{precip}}$ from the ensemble mean of three isotope-enabled Last Millennium Ensemble full-forcing simulations. Before determining the regression slopes, we calculated 30-year running means for both surface temperature and $\delta^{18}\text{O}_{\text{precip}}$ (Fig. 3). Regression slopes in the main text are reported for GMST vs two time series: global mean $\delta^{18}\text{O}_{\text{precip}}$ (using all grid cells) and mean $\delta^{18}\text{O}_{\text{precip}}$ calculated only for grid cells containing locations of Iso2k primary time series data contributing to the composites between 850 and 2000 CE.

Similarly, to estimate the amount of variance in individual Iso2k primary time series explained by proxy estimates of global temperature (Extended Data Fig. 6), we calculated R^2 for the 30-year binned data across the interval 1–2,000, ignoring bins that contained no observations. Correlations were calculated only if at least six bins overlapped the bins from the GMST reconstruction.

Calculation of relative humidity normalized to SST

Relative humidity was calculated from iCESM experiments for all grid points over the oceans from 60° N–60° S, that is, the portion of the lower troposphere receiving the majority of evaporated water from the surface oceans. RH_{SST} in Fig. 3 was calculated as the relative humidity of the surface-most model layer, normalized to the saturation vapour pressure at the temperature of the surface ocean rather than the air, following the physical principles of the Craig–Gordon model for an evaporating water body^{13,29,30}. All global mean time series in Fig. 3 are area weighted.

Calculation of trends

Trends (Fig. 2) were calculated as the slope of the linear regression from 850 to 1840 for a subset of Iso2k records meeting the following criteria: (1) designated ‘primary time series’, (2) containing at least one data point in the first and last 50 years of the time interval and (3) containing at least 20 data points over the full time interval (that is, ≥ 50 -year average resolution). For iCESM data, trends were calculated as the slope of the linear regression for monthly data covering the 850–1850 and 1850–2005 time intervals.

200-year standardized anomalies

We created standardized anomaly (‘zscore’) maps to aid interpretation of temporal variability in the composite time series (Extended Data Fig. 7). Similarly to the analyses described above, we filtered the database to include only the ‘primary’ isotope ($\delta^{18}\text{O}$ or $\delta^2\text{H}$) time series for each site and then grouped records according to the primary driver of isotopic variability. We then filtered this subset of datasets to include only records spanning >600 years within the CE. We averaged those records into 200-year bins and then calculated z-scores for each bin by subtracting the mean of all data points within the CE from the bin average and then dividing by the standard deviation of all data points within the CE. We performed this analysis using both ‘odd’ (100, 300, 500 and so on) and ‘even’ (200, 400, 600) centuries as bin centres and showed only the time periods relevant to the main text in Extended Data Fig. 7.

Data availability

The Iso2k Database⁵⁷ is available for download at <https://doi.org/10.25921/57j8-vs18> and is accessible via the NOAA/WDS Paleo Data landing page at <https://www.ncdc.noaa.gov/paleo/study/29593>. Composites and principal component datasets generated for this paper are available through GitHub at <https://github.com/nickmckay/iso2kNatureGeoscience2023> and archived via Zenodo (<https://doi.org/10.5281/zenodo.8327339>).

Code availability

Codes to reproduce the main results from this paper are available through GitHub at <https://github.com/nickmckay/iso2kNatureGeoscience2023> and archived via Zenodo (<https://doi.org/10.5281/zenodo.8327339>).

References

51. Cheng, H. et al. Ice age terminations. *Science* **326**, 248–252 (2009).
52. Wang, Y. J. et al. A high-resolution absolute-dated Late Pleistocene monsoon record from Hulu Cave, China. *Science* **294**, 2345–2348 (2001).
53. Dayem, K. E., Molnar, P., Battisti, D. S. & Roe, G. H. Lessons learned from oxygen isotopes in modern precipitation applied to interpretation of speleothem records of paleoclimate from eastern Asia. *Earth Planet. Sci. Lett.* **295**, 219–230 (2010).
54. Osman, M. B., Coats, S., Das, S. B., McConnell, J. R. & Chellman, N. North Atlantic jet stream projections in the context of the past 1,250 years. *Proc. Natl Acad. Sci. USA* **118**, e2104105118 (2021).
55. Hendricks, M. B., DePaolo, D. J. & Cohen, R. C. Space and time variation of $\delta^{18}\text{O}$ and δD in precipitation: can paleotemperature be estimated from ice cores? *Glob. Biogeochem. Cycles* **14**, 851–861 (2000).
56. Liu, Z. et al. Younger Dryas cooling and the Greenland climate response to CO_2 . *Proc. Natl Acad. Sci. USA* **109**, 11101–11104 (2012).
57. Konecky, B. L. & McKay, N. P. NOAA/WDS Paleoclimatology—The Iso2k Database (NOAA National Centers for Environmental Information, 2020); <https://doi.org/10.25921/57j8-vs18>
58. Craig, H. Isotopic variations in meteoric waters. *Science* **133**, 1702–1703 (1961).
59. Beckers, J.-M., Barth, A. & Alvera-Azcárate, A. DINEOF reconstruction of clouded images including error maps—application to the sea-surface temperature around Corsican Island. *Ocean Sci.* **2**, 183–199 (2006).
60. Alvera-Azcárate, A., Barth, A., Sirjacobs, D., Lenartz, F. & Beckers, J.-M. Data Interpolating Empirical Orthogonal Functions (DINEOF): a tool for geophysical data analyses. *Mediterr. Mar. Sci.* **12**, 5–11 (2011).
61. Oksanen, J. et al. Vegan: Community ecology package. R version 2.2.1 (2015); <https://cran.r-project.org/web/packages/vegan/index.html>
62. Wong, T. E., Nusbaumer, J. & Noone, D. C. Evaluation of modeled land–atmosphere exchanges with a comprehensive water isotope fractionation scheme in version 4 of the Community Land Model. *J. Adv. Model. Earth Syst.* **9**, 978–1001 (2017).
63. Allan, R. & Ansell, T. A new globally complete monthly historical gridded mean sea level pressure dataset (HadSLP2): 1850–2004. *J. Clim.* **19**, 5816–5842 (2006).

Acknowledgements

Iso2k is a contribution to Phase 3 and 4 of the PAGES 2k Network. PAGES received support from the Swiss Academy of Sciences, the US National Science Foundation and the Chinese Academy of Sciences. Support for this work includes NSF-AGS 1805141, NSF-AGS PRF 1433408 and a David and Lucile Packard Foundation Fellowship in Science and Engineering to B.L.K.; NSF-1948746 to N.P.M.; Australian Research Council through a Discovery Project (DP170100557) and the Centre of Excellence for Climate Extremes (CE170100023) to G.M.F.; NSF-AGS 1805143 and NSF-OCE-2202794 to S.L.S.; NSF-CAREER 2145725, NSF 2103035 and NSF 2002444 to A.R.A.; NSF-CAREER 1945479, NSF 1931242 and NSF 2002460 to D.M.T.; Australian Research Council Discovery Project DP190102782 to J.J.T.; South Central Climate Adaptation Science Center Cooperative Agreement G19AC00086, NSF-2102931 and NSF-1805702 to K.L.D.; RYC-2013-14073 programme and LINKA20102 and CEX2018-000794-S projects to B.M.; NSF-EAR PRF 1349595, NSF-EAR-IF 1652274, NSF-OPP 1504267, NSF-OPP 1737716 and NSF-CAREER 2044616 to E.K.T.; NSF-CAREER 1847791 to J.L.C.; National Oceanic and Atmospheric Administration award number NA18OAR4310427 to S.G.D.; PalMod, the German palaeoclimate modelling initiative, part of the Research for Sustainable

Development initiative funded by the German Federal Ministry of Education and Research (BMBF; 01LP1922A) to L.J.; RSF project 21-17-00006 to O.V.C.(S.); German Research Foundation grants OP217/2-1, OP217/3-1, OP217/4-1 to T.O.; Natural Sciences and Engineering Research Council of Canada Discovery Grant RGPIN-2016-06730 to T.J.P.; Australian Research Council Project (LP210300691) to G.S.; Australian Research Council through a Future Fellowship (FT160100029), Special Research Initiative for the Australian Centre for Excellence in Antarctic Science (SR200100008) and the Centre of Excellence for Climate Extremes (CE170100023) to N.J.A; Natural Sciences and Engineering Research Council of Canada Discovery Grant RGPIN-2021-03888 to A.J.O.; and Australian Antarctic Science (AAS) grants 757, 4061, 4062 and 4537 to M.C. and A.M.

Author contributions

Analyses presented in the main text and extended data were conceived and performed by B.L.K., N.P.M., G.M.F., S.L.S., M.J.F., A.R.A., D.M.T., M.D.J., J.J.T., E.K.T., J.L.C., S.G.D. and L.J. Results were analysed and interpreted by B.L.K., N.P.M., G.M.F., S.L.S., M.J.F., A.R.A., D.M.T., M.D.J., K.L.D., J.J.T., B.M. and E.K.T., with input from all authors. The manuscript was written mainly by B.L.K., N.P.M., G.M.F., S.L.S., M.J.F., A.R.A., D.M.T., M.D.J., K.L.D., J.J.T., B.M., E.K.T., J.L.C., S.G.D., L.J.

and H.R.S., with additional contributions from O.V.C.(S.), Z.K., T.O., T.J.P. and G.S. All Iso2k project members created the Iso2k database and edited the manuscript. B.L.K. directed the project, led the overall design of the study and led the writing of the manuscript.

Competing interests

The authors declare no competing interests.

Additional information

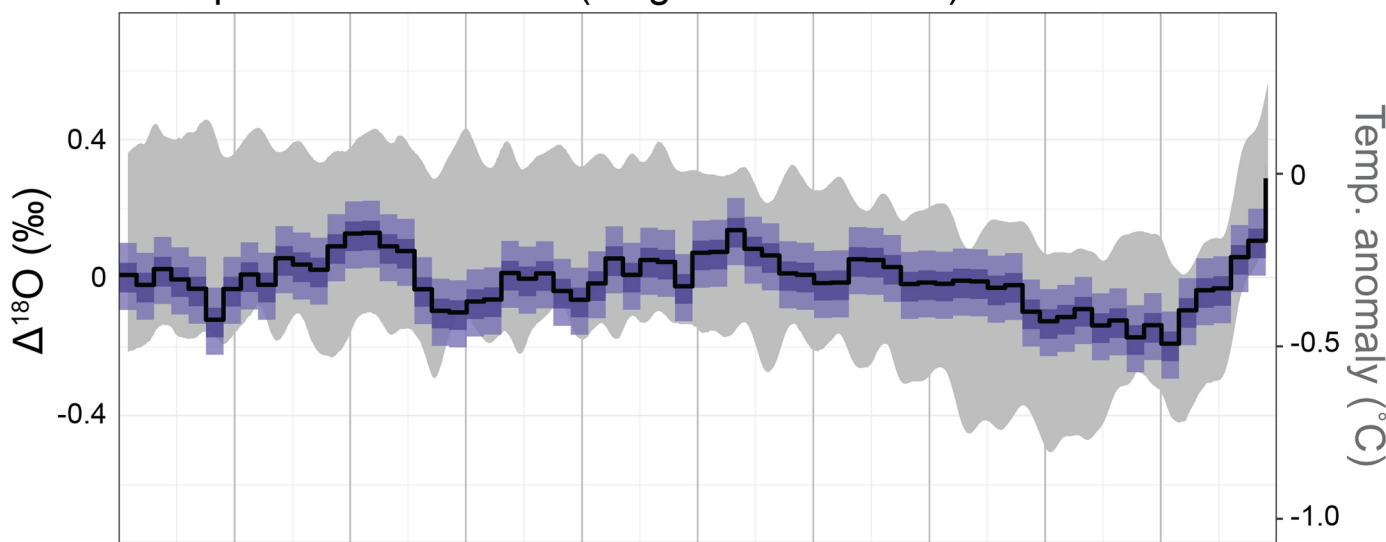
Extended data is available for this paper at
<https://doi.org/10.1038/s41561-023-01291-3>.

Correspondence and requests for materials should be addressed to Bronwen L. Konecky.

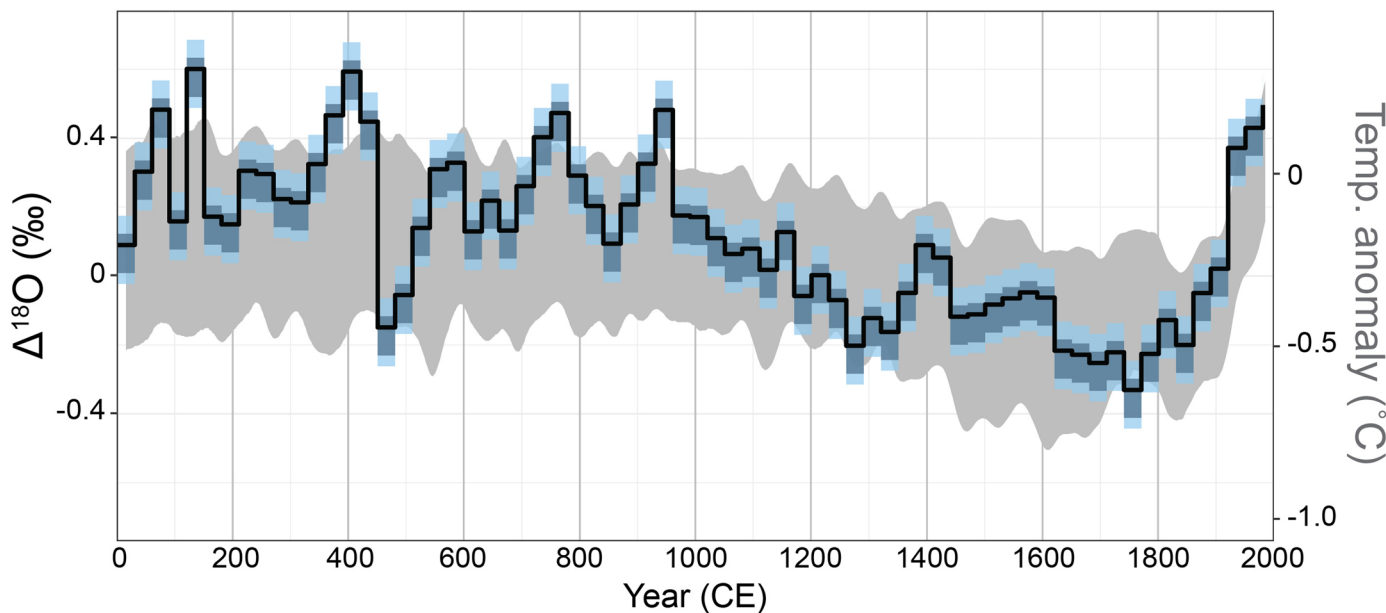
Peer review information *Nature Geoscience* thanks the anonymous reviewers for their contribution to the peer review of this work. Primary Handling Editor: James Super, in collaboration with the *Nature Geoscience* team.

Reprints and permissions information is available at
www.nature.com/reprints.

a Precipitation $\delta^{18}\text{O}$ or $\delta^2\text{H}$ (no glacier ice cores)

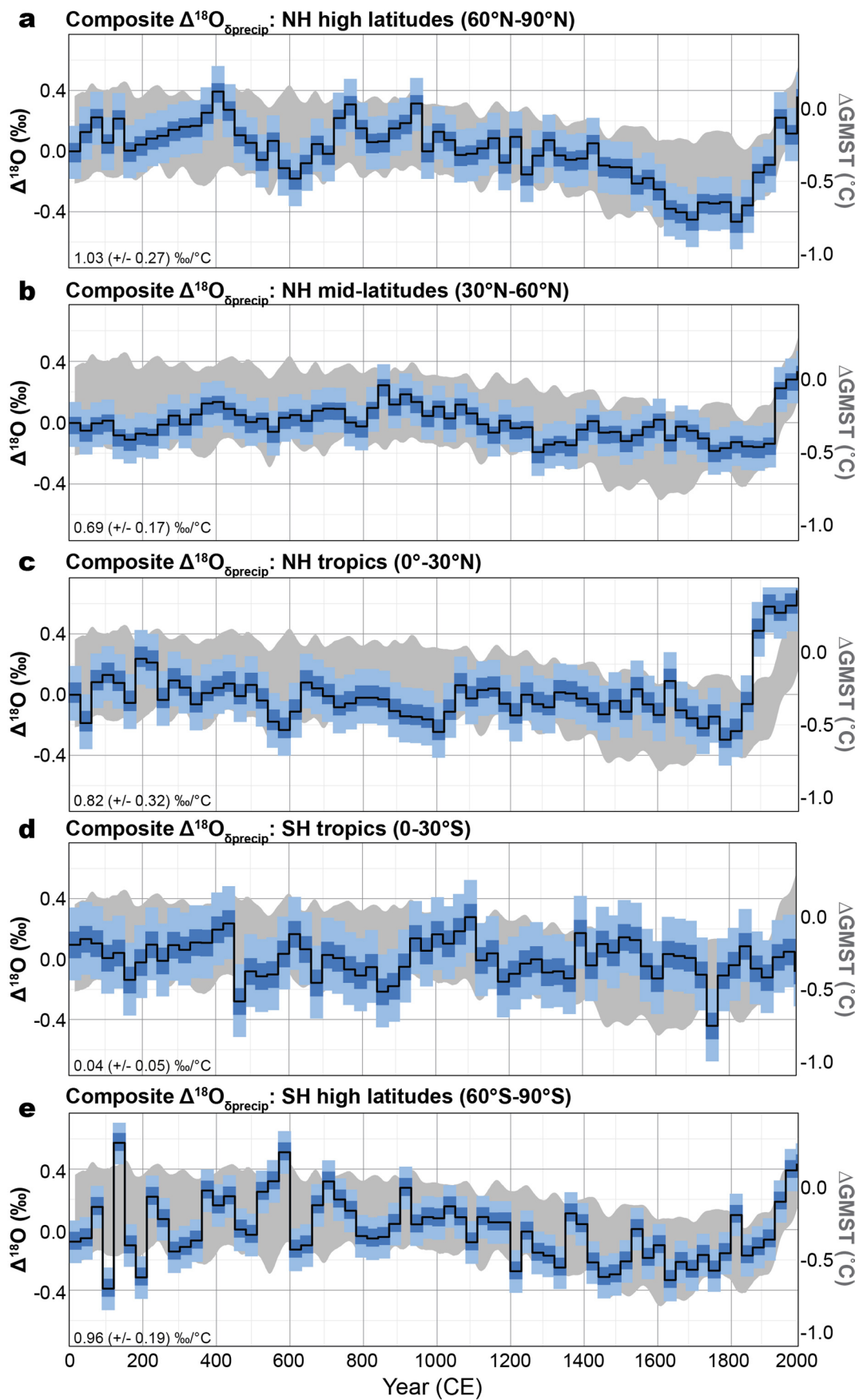


b Precipitation $\delta^{18}\text{O}$ or $\delta^2\text{H}$ (only glacier ice cores)



Extended Data Fig. 1 | Composite $\Delta^{18}\text{O}_{\text{precip}}$ calculated with and without glacier ice records. As per Fig. 1, the black line with coloured shading shows the 30-year binned proxy $\delta^{18}\text{O}$ anomaly from Iso2k records¹⁵ (black line, ensemble median; dark shading, first and third quantiles; light shading, 2.5th/97.5th percentiles). **(a)** Composite of $\Delta^{18}\text{O}_{\text{precip}}$ records from all archives other than glacier ice. **(b)** Composite of only glacier ice records. Records contributing to

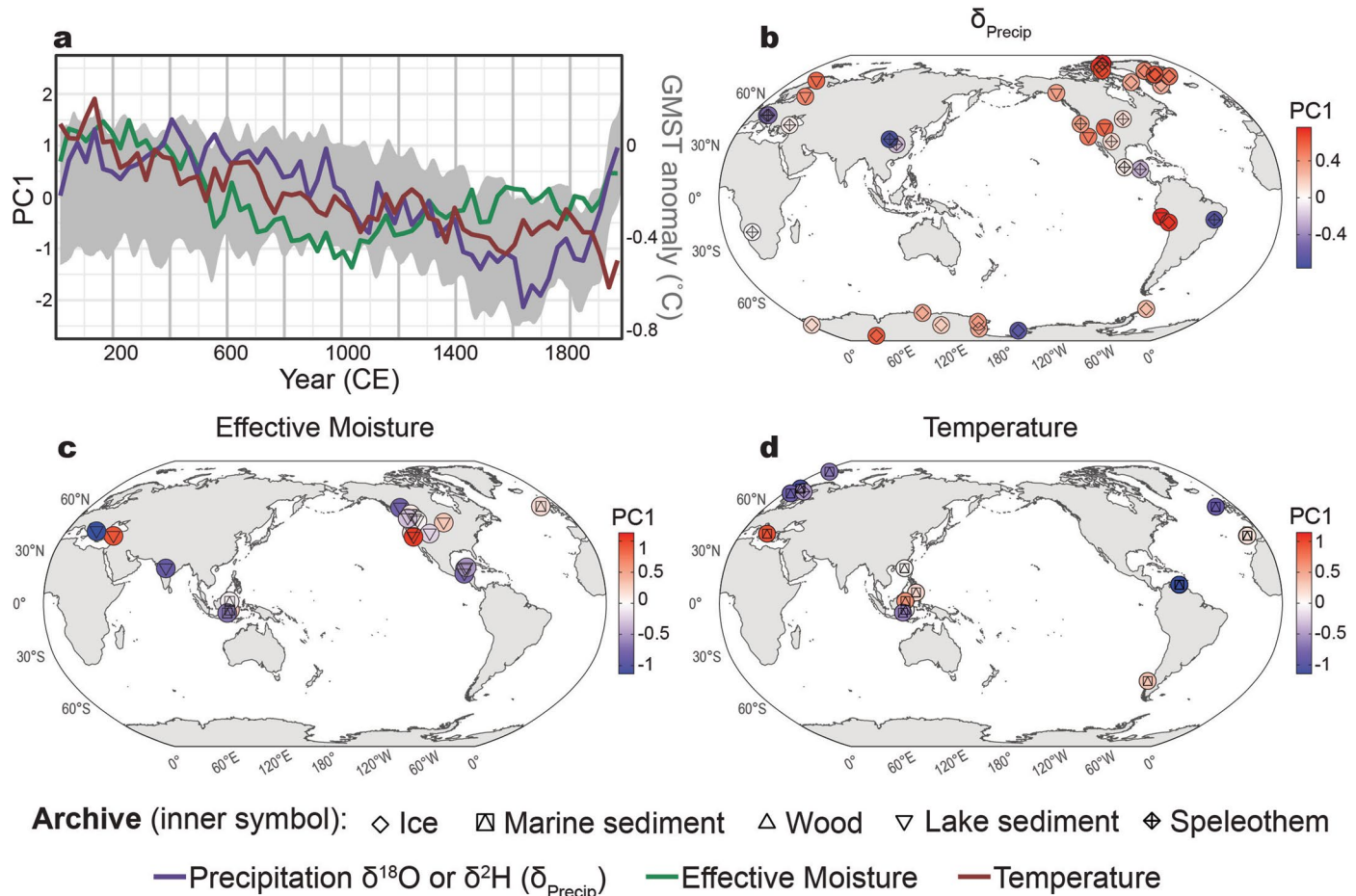
each bin are mean-centered but not scaled according to that record's variance (see Methods). Anomalies are in % relative to the 2000-year mean. Gray shading depicts the ensemble 2.5 and 97.5 percentile of the 31-year Butterworth-filtered Global Mean Surface Temperature (GMST) anomaly relative to the 1961-1990 mean¹.



Extended Data Fig. 2 | See next page for caption.

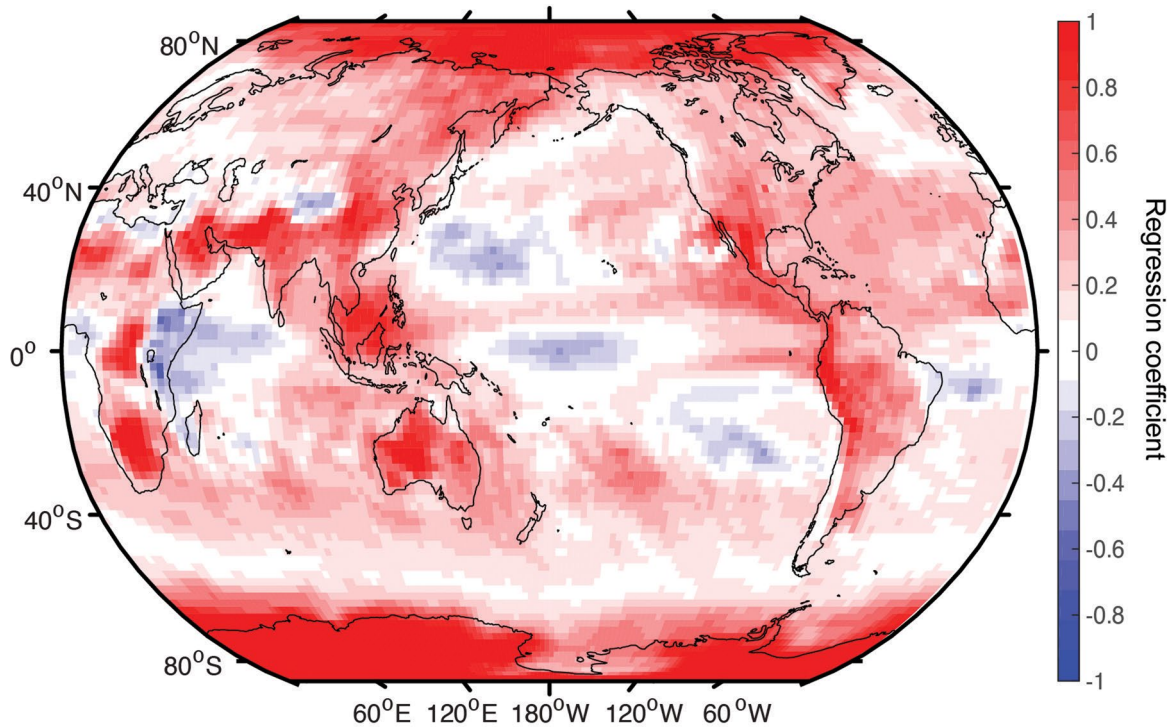
Extended Data Fig. 2 | Composite $\Delta^{18}\text{O}_{\text{precip}}$ calculated using Iso2k records¹⁵ falling within 30-degree latitudinal bins. **a**, 60–90°N ($n = 76$); **b**, 30–60°N ($n = 86$); **c**, 0–30°N ($n = 27$); **d**, 0–30°S ($n = 39$); **e**, 60–90°S ($n = 77$). As per Fig. 1, black line with coloured shading shows the 30-year binned proxy $\delta^{18}\text{O}$ anomaly (black line, ensemble median; dark shading, first and third quantiles; light shading, 2.5th/97.5th percentiles) and gray shading depicts the ensemble 2.5

and 97.5 percentile of the 31-year Butterworth-filtered GMST anomaly relative to the 1961–1990 mean¹. Black text denotes mean regression slope (± 1 standard deviation) of regional composite $\Delta^{18}\text{O}$ vs. GMST from 850–2000. Regional composite for 30–60°S not calculated due to insufficient number of records from those latitudes ($n = 2$).



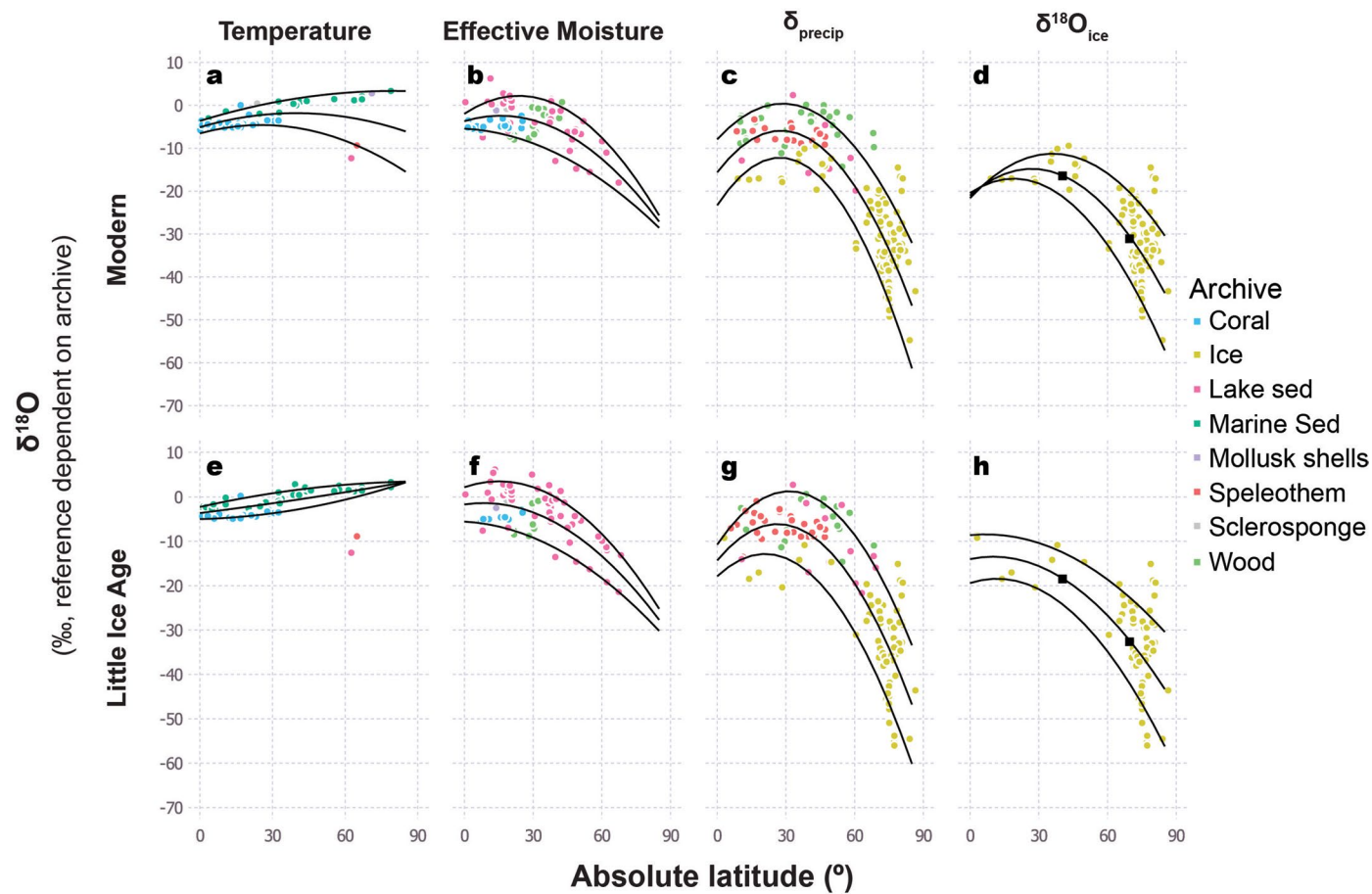
Extended Data Fig. 3 | First Principal Component (PC1) of Iso2k¹⁵ records during the full Common Era. Panels a–d, as in Fig. 2a–d but for the interval 0–1980 (30-year bins), and without trends depicted (that is, constant shape for outer symbols). δ_{precip} PC1 explains 19% of the total variance ($n = 44$). Effective

Moisture PC1 explains 19% of the total variance ($n = 19$). Temperature PC1 explains 25% of the total variance ($n = 19$). Maps created in R using coastlines from Natural Earth.

**Extended Data Fig. 4 | iCESM relationship between GMST and grid cell-level**

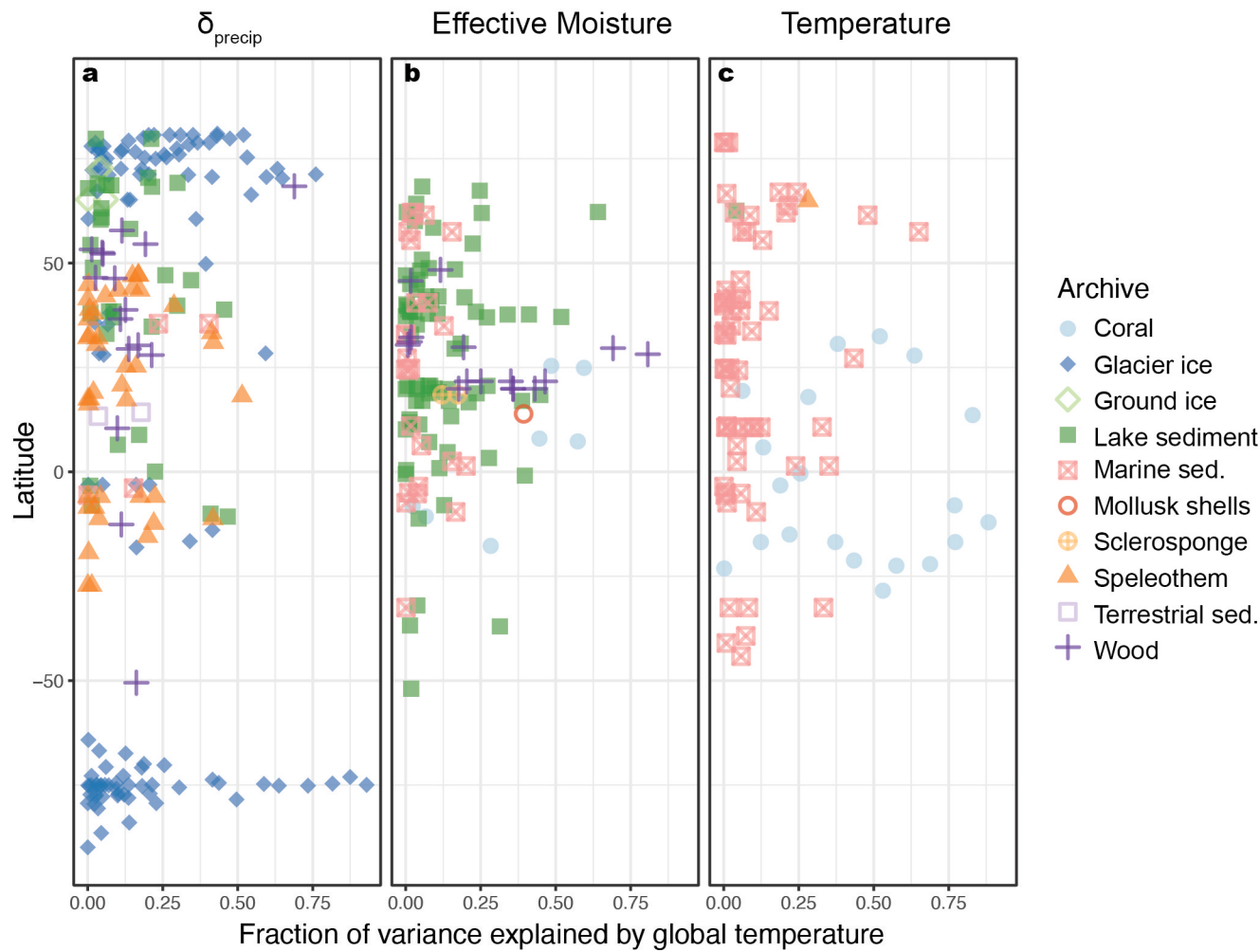
$\delta^{18}\text{O}_{\text{precip}}$. Shading depicts the regression coefficient in ‰/°C between mean annual, amount-weighted, 30-year running mean $\delta^{18}\text{O}_{\text{precip}}$ at every grid cell

vs. 30-year running mean, area-weighted GMST for the mean of 3 full-forcing, isotope-enabled Last Millennium Ensemble members^{18–20}. Map created in MATLAB using m_map for coastlines.



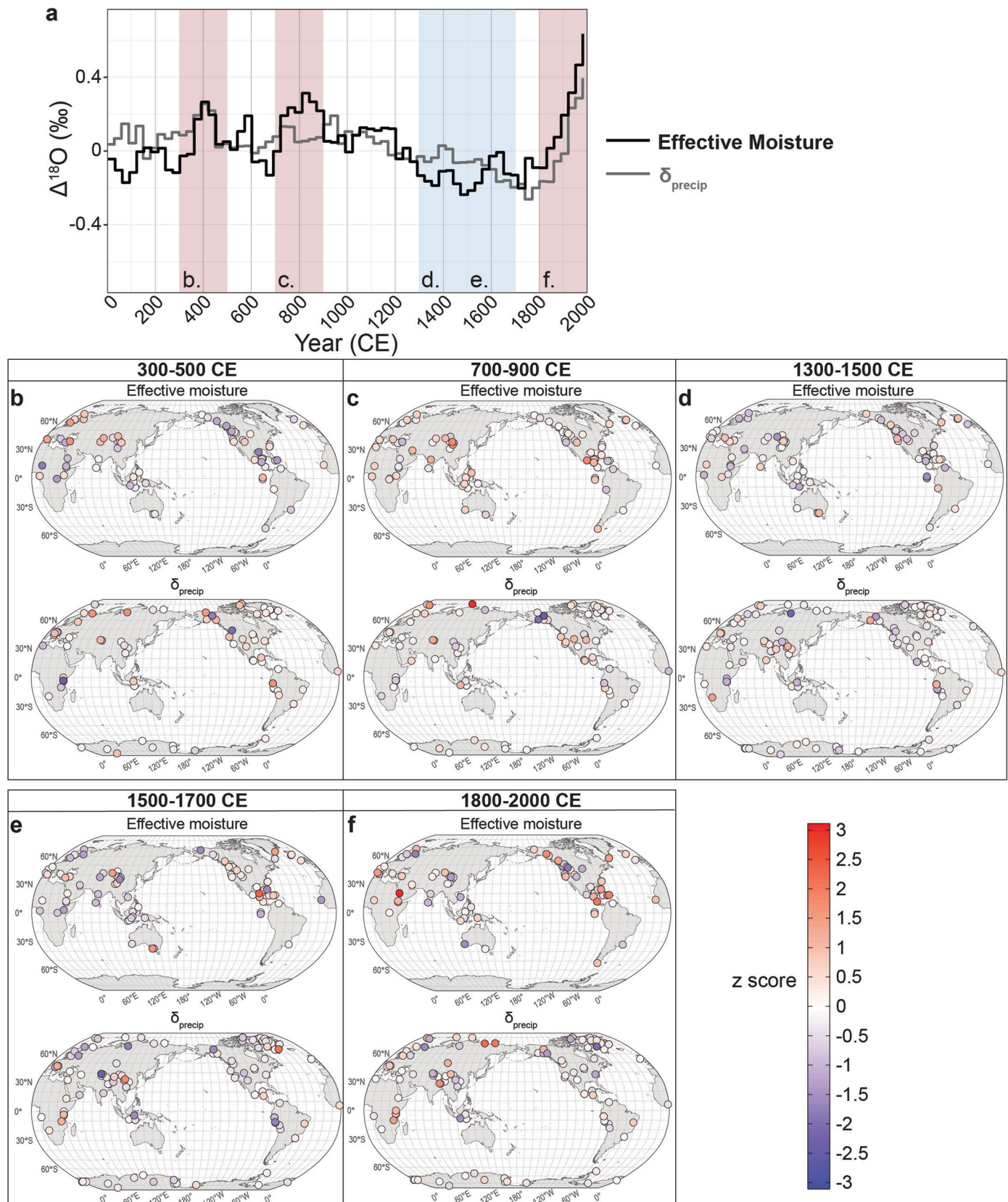
Extended Data Fig. 5 | $\delta^{18}\text{O}$ vs. latitude in the Iso2k database¹⁵ for the modern era (a-d; 1950-2018) and the Little Ice Age (e-h; 1450-1850). Data are plotted for the three main isotope interpretation categories (a-c, e-g) and for $\delta^{18}\text{O}$ of glacier and ground ice (d, h), the archives that preserve precipitation most directly. Black

squares on panels (d) and (h) indicate 40 and 70 degrees latitude, the interval for which the mean of the gradient function was calculated ($-0.48\text{‰}/^{\circ}$ latitude for both time periods; see main text). All records are plotted in permil on the VSMOW-SLAP scale for ice core records; PDB or VPDB for all other archives).



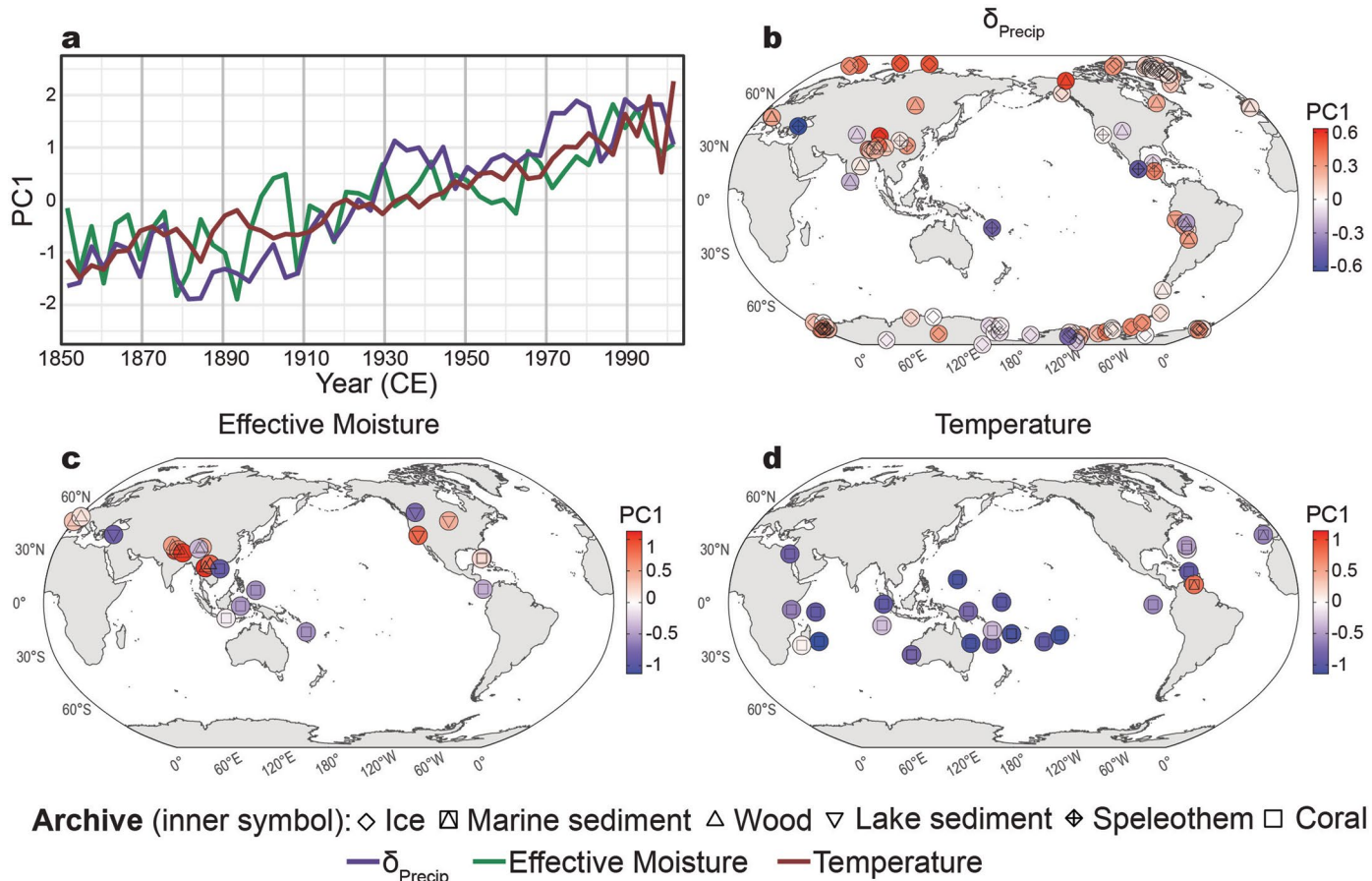
Extended Data Fig. 6 | Relation between Iso2k¹⁵ primary time series and Global Mean Surface Temperature (GMST). (a) Fraction of variance explained (R^2) in δ_{precip} primary time series by changes in PAGES 2k global mean surface temperature (GMST) over the past 2000 years^{1,2}. Both Iso2k time series and GMST

were averaged into 30 year bins before calculating correlations (See Methods). (b) As in (a), but for Effective Moisture primary time series. (c) As in (a), but for Temperature primary time series.



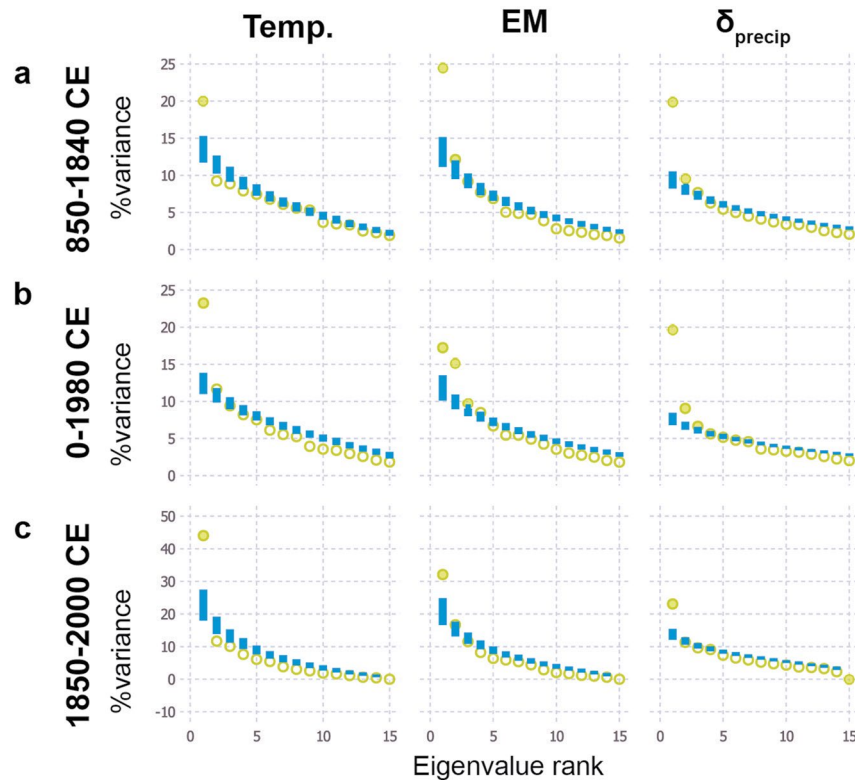
Extended Data Fig. 7 | Standardized 200-year $\delta^{18}\text{O}$ anomalies from Effective Moisture and δ_{precip} records. **a**, Composite medians for Iso2k¹⁵ Effective Moisture and δ_{precip} driven records, as shown in Fig. 1 of the main text. Red shading denotes intervals of relatively high composite $\Delta^{18}\text{O}_{\text{EM}}$, and blue shading denotes intervals of relatively low composite $\Delta^{18}\text{O}_{\text{EM}}$. **b-f**, Isotopic anomalies in individual

EM and δ_{precip} records contributing to the composites during those shaded intervals, via standardised anomaly maps for time intervals discussed in the main text (see Methods). These maps only include records with data spanning ≥ 600 years. Standardized anomalies at each site are relative to the Common Era mean value for that record. Maps created in R using coastlines from Natural Earth.



Extended Data Fig. 8 | First Principal Component (PC1) of Iso2k¹⁵ data for the Historical Period. Panels a–d, as in Extended Data Fig. 3a–d, but for the interval 1850–2005, with 3-year bins. δ_{precip} PC1 explains 12% of the total variance ($n = 109$).

Effective Moisture PC1 explains 32% of the total variance ($n = 29$). Temperature PC1 explains 38% of the total variance ($n = 27$). Maps created in R using coastlines from Natural Earth.



Extended Data Fig. 9 | Significance of Iso2k¹⁵ PCA eigenvalues with respect to a null hypothesis of stochastic forcing with decadal persistence. **a**, Block bootstrap results from 850–1840 with a 30-year bin width, 10-year block length, and tolerance of up to 15% missing data (that is, 85% coverage during the time interval; Methods). Yellow symbols depict the eigenvalues (expressed as a percentage of the total variance) of each principal component. Blue bars show

the 1–99% confidence intervals of the stochastic null hypothesis ($n = 1000$). Eigenvalues above the 99% confidence interval are significant at the 1% level (one-sided test) and therefore are unlikely to have arisen stochastically, and unlikely to be an artifact of the data processing steps (that is, binning and interpolation). **(b)** as in **(a)** but for 0–1980. **(c)** as in **(a)** but for 1850–2000 and with a 10-year bin width and tolerance of up to 10% missing data (90% coverage).